

N-BODY SIMULATIONS FOR EXTENDED QUINTESSENCE MODELS

BAOJIU LI^{1,2}, DAVID F. MOTA³ AND JOHN D. BARROW²

¹DAMTP, Centre for Mathematical Sciences, University of Cambridge, Wilberforce Road, Cambridge CB3 0WA, UK

²Kavli Institute for Cosmology Cambridge, Madingley Road, Cambridge CB3 0HA, UK and

³Institute of Theoretical Astrophysics, University of Oslo, 0315 Oslo, Norway

Draft version November 10, 2021

ABSTRACT

We introduce the N -body simulation technique to follow structure formation in linear and nonlinear regimes for the extended quintessence models (scalar-tensor theories in which the scalar field has a self-interaction potential and behaves as dark energy), and apply it to a class of models specified by an inverse power-law potential and a non-minimal coupling. Our full solution of the scalar field perturbation confirms that, when the potential is not too nonlinear, the effects of the scalar field could be accurately approximated as a modification of background expansion rate plus a rescaling of the effective gravitational constant relevant for structure growth. For the models we consider, these have opposite effects, leading to a weak net effect in the linear perturbation regime. However, on the nonlinear scales the modified expansion rate dominates and could produce interesting signatures in the matter power spectrum and mass function, which might be used to improve the constraints on the models from cosmological data. We show that the density profiles of the dark matter halos are well described by the Navarro-Frenk-White formula, although the scalar field could change the concentration. We also derive an analytic formula for the scalar field perturbation inside halos assuming NFW density profile and sphericity, which agrees well with numerical results if the parameter is appropriately tuned. The results suggest that for the models considered, the spatial variation of the scalar field (and thus the locally measured gravitational constant) is very weak, and so local experiments could see the background variation of gravitational constant.

1. INTRODUCTION

The nature of the dark energy (Copeland, Sami & Tsujikawa 2006) is one of the most difficult challenges facing physicists and cosmologists now. Although a cosmological constant (plus cold dark matter, to provide the concordance Λ CDM paradigm) could be a solution – and is indeed consistent with virtually all current observations, it suffers from theoretical difficulties such as why its value must be so small yet non-zero, and why it becomes dominant only at the low redshift. In all the alternative proposals to tackle this problem, a quintessence scalar field (Zlatev, Wang & Steinhardt 1999; Wang *et al.* 2000) is perhaps the most popular one (although a new proposal by Barrow & Shaw (2010) provides a completely new type of explanation that does not require new scalar fields). In such models the scalar field φ is slowly rolling down its potential, its energy density is dominated by the potential energy and almost remaining constant provided that the potential is flat enough. The flatness of the potential, however, means that the mass of the scalar field is in general very light and as a result the scalar field almost does not cluster so that its effects in cosmology are mainly on the (modified) background expansion rate.

One reason for the wide interest in quintessence models is that scalar fields appear in abundance in high-energy physics theories, in which they are often coupled to the curvature invariants or even other

matter species, leading to the so-called extended quintessence (Perrotta, Baccigalupi & Matarrese 2000; Baccigalupi & Perrotta 2000; Baccigalupi, Perrotta & Matarrese 2000) and coupled quintessence (Amendola 2000, 2004; Jesus *et al.* 2008) models respectively. The former is just a special class of a scalar-tensor theory (Fujii & Maeda 2003; Riazuelo & Uzan 2002), with the scalar field being the dark energy. These two classes of generalised quintessence models have been studied in detail in the linear regime in the literature (Bean 2001a,b; Mangano *et al.* 2003; Clifton, Mota & Barrow 2005; Nunes & Mota 2006; Pettorino, Baccigalupi & Mangano 2005; Koivisto 2005; Brookfield *et al.* 2006; Koivisto & Mota 2007; Mota & Shaw 2007, 2006; Lee, Liu & Ng 2006; Mota *et al.* 2007; Bean *et al.* 2008; Bean, Flanagan & Trodden 2008; Boehmer *et al.* 2008, 2010).

In recent years, studies of the cosmological behaviour of the coupled quintessence model in the nonlinear regime have also been made, either via semi-analytical methods (Manera & Mota 2006; Mota & van de Bruck 2004; Mota 2008; Shaw & Mota 2008; Mota *et al.* 2008a; Mota, Shaw & Silk 2008; Saracco *et al.* 2009; Wintgerst & Pettorino 2010), or using N -body simulation techniques (Maccio *et al.* 2004; Nusser, Gubser & Peebles 2005; Kesden & Kamionkowski 2006a,b; Springel & Farrar 2007; Farrar & Rosen 2007; Baldi & Pettorino 2010; Hellwing & Juszkiewicz 2009; Keselman, Nusser & Peebles 2009, 2010; Hellwing, Knollmann & Knebe 2010; Baldi 2010; Baldi *et al.* 2010). In these studies the effect of the

Email address: b.li@damtp.cam.ac.uk
Email address: d.f.mota@astro.uio.no
Email address: j.d.barrow@damtp.cam.ac.uk

scalar field is generally approximated by a Yukawa-type ‘fifth force’ or by a rescaling of the gravitational constant or the particle mass, without solving the scalar field equation explicitly. Very recently, [Li & Zhao \(2009, 2010\)](#); [Zhao *et al.* \(2010\)](#); [Li & Barrow \(2010\)](#) gave a new treatment and obtained an explicit solution to the scalar field perturbation on a spatial grid. The new results confirmed that the approximations adopted in the old literature were good for the models considered there (where the scalar potential was not very nonlinear), but for highly nonlinear potentials they broke down.

For the extended quintessence (more generally scalar-tensor) models, investigations using N -body simulations are rarer. The work of [Pettorino & Baccigalupi \(2008\)](#), for example, outlined a recipe which uses certain approximation, such as a rescaling of gravitational constant, and does not solve the scalar field equation of motion explicitly. In [Rodriguez-Meza *et al.* \(2007\)](#); [Rodriguez-Meza \(2008a,b\)](#), the authors approximated the effect of scalar field coupling as a Yukawa force. However, none of these previous works tries to solve the scalar field on a mesh directly, and this is what we want to do in this work.

The aims of this work are threefold. Firstly, we want to develop the formulae and methods that are needed to solve the scalar field explicitly, which could serve as the basis for future work, and to find the regime of validity of our method. Secondly, we want to understand whether the approximations adopted in the previous studies are good or not; given the severe limits in the computing power; if those approximations do work well, then one does not need to resort to an exact scalar field solver, which is considerably more economical. Finally, we want to study structure formation in the nonlinear regime for some specific models, and investigate both the scalar field effects on the clustering of matter and the spatial variation of the gravitational constant (which is common to scalar-tensor theories).

The organisation of this paper is as follows: In [Sect. 2](#) we list the basic equations which are needed in N -body simulations and give their respective non-relativistic limits. To prevent the main text from expanding too much, some useful expressions are listed in [Appendix A](#), and the discrete versions of the resulted equations are discussed and summarised in [Appendix B](#). In [Sect. 3](#) we briefly describe the numerical code we are using (relegating further details to [Knebe, Green & Binney \(2001\)](#); [Li & Zhao \(2010\)](#)), and the physical parameters of our simulations. We also present some results regarding the background cosmology and linear perturbation evolution in our models, which could be helpful in the understanding of the N -body simulation results (our algorithm for the background cosmology is summarized in [Appendix C](#)). [Sect. 4](#) contains the N -body simulation results, including key structure formation observables such as nonlinear matter power spectrum, mass function and dark matter halo profile, as well as the spatial variation of the scalar field. It also includes several checks of the approximations made in the literature. We finally summarise and conclude in [Sect. 5](#).

We use the unit $c = 1$ unless explicitly restoring c in the equations. The metric convention is $(+, -, -, -)$. Indices a, b, c, \dots run $0, 1, 2, 3$ while i, j, k, \dots run $1, 2, 3$.

2. THE EQUATIONS

This section presents the equations that will be used in the N -body simulations, the model parameterisation and discretisation procedure for the equations.

2.1. The Basic Equations

We consider a general Lagrangian density for scalar-tensor theories

$$\mathcal{L} = \frac{1}{2\kappa_*} [1 + f(\varphi)] R - \frac{1}{2} \nabla^a \varphi \nabla_a \varphi + V(\varphi) - \mathcal{L}_f, \quad (1)$$

in which $\kappa_* = 8\pi G_*$ where G_* is the (bare) gravitational constant, R is the Ricci scalar, $f(\varphi)$ is the coupling function between the scalar field φ and curvature, $V(\varphi)$ the potential for φ and \mathcal{L}_f the Lagrangian density for fluid matter (baryons, photons, neutrinos and cold dark matter). Note that G_* is a fundamental constant of the theory.

Varying the associated action with respect to metric g_{ab} yields the energy-momentum tensor of the theory (note the tilde, which is used to distinguish it from the T_{ab} defined below):

$$\begin{aligned} \tilde{T}_{ab} = & T_{ab}^f + \nabla_a \nabla_b \varphi - \frac{1}{2} g_{ab} \nabla^c \varphi \nabla_c \varphi + g_{ab} V(\varphi) \\ & - \frac{1}{\kappa_*} [f(\varphi) G_{ab} + (g_{ab} \nabla^c \nabla_c - \nabla_a \nabla_b) f(\varphi)] \quad (2) \end{aligned}$$

where $G_{ab} = R_{ab} - \frac{1}{2} g_{ab} R$ is the Einstein tensor, and T_{ab}^f is the energy-momentum tensor for matter (including baryons, dark matter, neutrinos and photons, which we collectively refer to as ‘fluid matter’, although in N -body simulations we use discrete particles rather than a fluid).

As usual, we can rearrange the Einstein equation as

$$G_{ab} = \kappa_* \tilde{T}_{ab} \quad (3)$$

so that it now looks like

$$\begin{aligned} G_{ab} = & \frac{\kappa_*}{1+f} T_{ab}^f - \frac{1}{1+f} (g_{ab} \nabla^c \nabla_c - \nabla_a \nabla_b) f \\ & + \frac{\kappa_*}{1+f} \left[\nabla_a \varphi \nabla_b \varphi - \frac{1}{2} g_{ab} (\nabla \varphi)^2 + g_{ab} V \right] \\ \equiv & \kappa_* T_{ab}. \quad (4) \end{aligned}$$

Note the difference between T_{ab}^f and T_{ab} ; throughout this paper, we will use a superscript f for normal fluid matter, and quantities without a superscript f always mean the total effective ones [the final line of [Eq. \(4\)](#)]. It is sometimes useful to define an effective Newton constant $\kappa_{eff} \equiv \kappa_*/(1+f)$. Neither κ_* nor κ_{eff} is the gravitational constant measured in a Cavendish-type experiment, which we denote instead by κ_{\oplus} and is given by

$$\kappa_{\oplus} = \frac{\kappa_*}{1+f} \frac{2 + 2f + 4 \left(\frac{df}{d\sqrt{\kappa_*} \varphi} \right)^2}{2 + 2f + 3 \left(\frac{df}{d\sqrt{\kappa_*} \varphi} \right)^2} \quad (5)$$

where $\sqrt{\kappa_*}$ is added to make $\sqrt{\kappa_*} \varphi$ dimensionless, which is the convention we shall always follow below. κ_{\oplus} itself is obviously not a constant and we measure only its present-day value, $\kappa_{\oplus 0}$.

Varying the action with respect to the scalar field, φ , gives the scalar field equation of motion

$$\nabla^a \nabla_a \varphi + \frac{\partial V(\varphi)}{\partial \varphi} + \frac{R}{2\kappa_*} \frac{\partial f(\varphi)}{\partial \varphi} = 0. \quad (6)$$

Since we will follow the motions of dark matter particles in the N -body simulations, so we also need their geodesic equation. The dark-matter Lagrangian for a point particle with mass m_0 is

$$\mathcal{L}_{\text{CDM}}(\mathbf{y}) = -\frac{m_0}{\sqrt{-g}} \delta(\mathbf{y} - \mathbf{x}_0) \sqrt{g_{ab} \dot{x}_0^a \dot{x}_0^b}, \quad (7)$$

where \mathbf{y} is the general coordinate and \mathbf{x}_0 is the coordinate of the centre of the particle. From this equation we derive the corresponding energy-momentum tensor:

$$T_{\text{CDM}}^{ab} = \frac{m_0}{\sqrt{-g}} \delta(\mathbf{y} - \mathbf{x}_0) \dot{x}_0^a \dot{x}_0^b. \quad (8)$$

Taking the conservation equation for dark matter particles (which, unlike in (Li & Zhao 2009, 2010), does not couple to any other matter species, including the scalar field φ), the geodesic equation follows as usual:

$$\ddot{x}_0^a + \Gamma_{bc}^a \dot{x}_0^b \dot{x}_0^c = 0, \quad (9)$$

where the second term on the left-hand side accounts for gravity.

Eqs. (4, 6, 9) contain all the physics needed for the following analysis, though certain approximations and simplifications might have to be made in due course to make direct connection to N -body simulations.

We will consider an inverse power-law potential for the scalar field,

$$V(\varphi) = \frac{\Lambda^4}{(\sqrt{\kappa_*} \varphi)^\alpha}, \quad (10)$$

where α is a dimensionless constant and Λ is a constant with dimensions of mass. This potential has also been adopted in various background or linear perturbation studies of scalar fields (either minimally or non-minimally coupled); the tracking behaviour it produces makes it a good dark energy candidate and for that purpose we shall choose $\alpha \sim \mathcal{O}(0.1 - 1)$. Meanwhile, the coupling between the scalar field and the curvature tensor is chosen to be a non-minimal one:

$$f(\varphi) = \gamma \kappa_* \varphi^2, \quad (11)$$

where γ is another dimensionless constant characterising the strength of the coupling. Note that here again κ_* is added into $f(\varphi)$ and $V(\varphi)$ to make a dimensionless quantity $\sqrt{\kappa_*} \varphi$. Although the exact value of κ_* is unknown, so is φ and we can solve for $\sqrt{\kappa_*} \varphi$ instead of φ , not caring about the exact individual values of $\sqrt{\kappa_*}$ and φ .

2.2. The Non-Relativistic Limits

The N -body simulation only probes the motion of particles at late times, and we are not interested in extreme conditions such as black hole formation and evolution, so we can take the non-relativistic limit of the above equations as a good approximation.

The existence of the scalar field and its coupling to the curvature leads to several possible changes with respect to the Λ CDM paradigm:

1. The scalar field has its own energy-momentum tensor, which could change the source term of the Poisson equation because the scalar field, unlike the cosmological constant, can cluster (though the clustering is often quite weak in scalar field models). Also, unlike in coupled scalar field models, here the $\vec{\nabla}^2 \varphi$ term will appear in the Poisson equation.
2. The background cosmic expansion rate is in general modified, and can either slow down or speed up the rate of structure formation.
3. The two gravitational potentials in the conformal Newtonian gauge metric $ds^2 = a^2(1 + 2\phi)d\tau^2 + a^2(1 - 2\psi)\delta_{ij}dx^i dx^j$, in which τ and x^i are respectively the conformal time and comoving coordinate, are no longer equal to each other (as in general relativity), but are instead related by $\vec{\nabla}^2 \varphi$ (see below).

It therefore becomes clear that the following two equations, in their non-relativistic forms, need to be solved in order to obtain the gravitational force on particles:

1. The scalar field equation of motion, which is used to compute *explicitly* the value of the scalar field φ at any given time and position;
2. The Poisson equation, which is used to determine the gravitational potential and force at any given time and position from the local energy density and pressure, which includes the contribution from the scalar field (obtained from the φ equation of motion).

Note that unlike in the coupled scalar field models, there is no fifth force because there is no direct coupling to the particles. The scalar coupling to the curvature, however, does modify the gravitational potential so that gravity no longer follows Einstein's prescription and so this is a modified gravity theory.

We now describe these two equations in turn. For the scalar field equation of motion, we denote by $\bar{\varphi}$ the background value of φ and write $\delta\varphi \equiv \varphi - \bar{\varphi}$. Then using the expressions given in Appendix A we write

$$a^2 \nabla^a \nabla_a \varphi = \varphi'' + 2\mathcal{H}\varphi' + \vec{\nabla}_{\mathbf{x}}^2 \varphi - 2\phi\varphi'' - (\phi' + 3\psi' + 4\mathcal{H}\phi)\varphi' \quad (12)$$

in which $' = d/d\tau$ with τ the conformal time, $\vec{\nabla}_{\mathbf{x}}$ is the derivative with respect to the comoving coordinate \mathbf{x} , and $\mathcal{H} = a'/a$. Then, with the background part subtracted, Eq. (6) can be rewritten as

$$\begin{aligned} \delta\varphi'' + 2\mathcal{H}\delta\varphi' + \vec{\nabla}_{\mathbf{x}}^2 \delta\varphi + [V_{,\varphi}(\varphi) - V_{,\varphi}(\bar{\varphi})] a^2 \\ - 2\phi\delta\varphi'' - (\phi' + 3\psi' + 4\mathcal{H}\phi)\delta\varphi' \\ + \frac{1}{2\kappa_*} [Rf_{\varphi}(\varphi) - \bar{R}f_{\varphi}(\bar{\varphi})] a^2 = 0, \end{aligned}$$

in which a bar denotes the background value, and the subscript $_{\varphi}$ denotes derivatives with respect to φ . Note that $\vec{\nabla}_{\mathbf{x}}^2$ has the same sign as $\vec{\nabla}_{\mathbf{r}}^2$.

In our N -body simulations we shall work in the quasi-static limit, *i.e.*, we assume that the spatial gradients are much greater than the time derivatives, $|\vec{\nabla}_{\mathbf{x}} \varphi| \gg |\frac{\partial \delta\varphi}{\partial \tau}|$.

Therefore, the time derivatives in the above equation are dropped and we obtain the simplified version

$$c^2 \bar{\partial}_{\mathbf{x}}^2 (a \delta \varphi) \quad (13)$$

$$= a^3 [V_{\varphi}(\varphi) - V_{\varphi}(\bar{\varphi})] + \frac{1}{2\kappa_*} [R f_{\varphi}(\varphi) - \bar{R} f_{\varphi}(\bar{\varphi})] a^3,$$

in which $\bar{\partial}_{\mathbf{x}}^2 = -\bar{\nabla}_{\mathbf{x}}^2 = +(\partial_x^2 + \partial_y^2 + \partial_z^2)$ due to our sign convention (+, -, -, -), and we have restored the factor c^2 in front of $\bar{\nabla}_{\mathbf{x}}^2$ (the φ here and in the remaining of this paper is c^{-2} times the φ in the original Lagrangian unless otherwise stated). Note that here V has the dimension of *mass* density rather than *energy* density.

To complete Eq. (13), we still need expressions for R and \bar{R} , which are again obtained using the quantities in Appendix A:

$$R = -\frac{6}{a^2} \frac{a''}{a} (1 - 2\phi) + \frac{1}{a^2} [6\psi'' + 6\mathcal{H}(\phi' + 3\psi') - 4\bar{\partial}_{\mathbf{x}}^2 \psi + 2\bar{\partial}_{\mathbf{x}}^2 \phi], \quad (14)$$

$$\bar{R} = -\frac{6}{a^2} \frac{a''}{a} \quad (15)$$

and so

$$R f_{\varphi} - \bar{R} \bar{f}_{\varphi} \doteq \bar{f}_{\varphi} \delta R + \bar{R} \delta f_{\varphi} \doteq -\frac{1}{a^2} \bar{f}_{\varphi} (4\bar{\partial}_{\mathbf{x}}^2 \psi - 2\bar{\partial}_{\mathbf{x}}^2 \phi) - \frac{6}{a^2} \frac{a''}{a} \delta f_{\varphi} \quad (16)$$

where we have again dropped time derivatives of ϕ and ψ since they are small compared with the corresponding spatial gradients, and $\delta R \equiv R - \bar{R}$, $\delta f_{\varphi} \equiv f_{\varphi} - \bar{f}_{\varphi}$.

Since only ϕ but not ψ appears in the Poisson equation (shown below), we also want to eliminate the ψ in the scalar field equation of motion. This is easy in general relativity, because there we have the simple relation $\phi = \psi$, which unfortunately no longer holds in scalar-tensor theories. However, we could use the $i-j$ components of the Einstein equation $G^i_j = \kappa_* T^i_j$ ($i \neq j$) to get a new relation between ϕ and ψ . Noting that our N -body simulations probe the very late time evolution (when radiation is negligible) when the only significant source for T^i_j ($i \neq j$) is the scalar field, and

$$\nabla^i \nabla_j f = -\frac{1}{a^2} \partial_i \partial_j f \quad (i \neq j) \quad (17)$$

where $\partial_i \equiv \partial/\partial x^i$, we could write the $i-j$ component of Einstein equation as

$$\partial_i \partial_j (\phi - \psi) = -\frac{c^2}{1+f} \partial_i \partial_j f$$

which gives approximately

$$\partial_i (\phi - \psi) = -\frac{c^2}{1+f} \partial_i f$$

and so

$$4\bar{\partial}_{\mathbf{x}}^2 \psi - 2\bar{\partial}_{\mathbf{x}}^2 \phi \doteq 2\bar{\partial}_{\mathbf{x}}^2 \phi + \frac{4}{1+f} \bar{\partial}_{\mathbf{x}}^2 f \doteq 2\bar{\partial}_{\mathbf{x}}^2 \phi + \frac{4\bar{f}_{\varphi}}{1+f} c^2 \bar{\partial}_{\mathbf{x}}^2 \delta \varphi. \quad (18)$$

It is important to note that in the second line of Eq. (18) we have implicitly linearised the equation; this is valid only if $f(\varphi)$ is not strongly nonlinear and $|\delta\varphi/\varphi| \ll 1$. It turns out that the model considered in this work satisfies these criteria ($f(\varphi) \propto \varphi^2$). If either $V(\varphi)$ or $f(\varphi)$ is highly nonlinear, then we might have $|\delta\varphi| \sim \varphi$; in that case we should not approximate f to \bar{f} even in the coefficients of the perturbation variables such as $\bar{\partial}_{\mathbf{x}}^2 \delta \varphi$ here, or write $\bar{\partial}_{\mathbf{x}}^2 f = \bar{f}_{\varphi} \bar{\partial}_{\mathbf{x}}^2 \delta \varphi$. The reason for the latter stricture is as follows: if $f(\varphi)$ is highly nonlinear, then f might change a lot even if φ fluctuates a little, implying that for the linearisation to apply on our spatial grid we need very small grid sizes which are impossible; moreover, it becomes complicated to decide which solution we should linearise around, as the values of f in that area which we look at might be very different from the background value \bar{f} . The strategy for this situation is simple: instead of writing $\bar{\partial}_{\mathbf{x}}^2 f = \bar{f}_{\varphi} \bar{\partial}_{\mathbf{x}}^2 \delta \varphi$, we difference $f(\varphi)$ directly, because we know the value of $f(\varphi)$ in every grid cell. This will ensure no linearisation error. In what follows, however, we shall use Eq. (18), which causes negligible linearisation error but simplifies the equations a lot. We shall also write $f \doteq \bar{f}$ in the coefficients of perturbation quantities such as $\bar{\partial}_{\mathbf{x}}^2 \delta \varphi$ and $\bar{\partial}_{\mathbf{x}}^2 \Phi$.

Substituting Eqs. (16, 18) into Eq. (13) and rearranging, we complete the derivation of the scalar field equation of motion in the weak field limit, ending up with

$$\left[1 + \frac{2\bar{f}_{\varphi}^2}{\kappa_* (1+f)} \right] c^2 \bar{\partial}_{\mathbf{x}}^2 (a \delta \varphi) = a^3 [V_{\varphi}(\varphi) - V_{\varphi}(\bar{\varphi})] - \frac{\bar{f}_{\varphi}}{2\kappa_*} \bar{\partial}_{\mathbf{x}}^2 \Phi - \frac{3}{\kappa_*} \frac{a''}{a} a \delta f_{\varphi} \quad (19)$$

for our general Lagrangian Eq. (1) and

$$\left[1 + \frac{8\gamma^2 \kappa_* \bar{\varphi}^2}{1 + \gamma \kappa_* \bar{\varphi}^2} \right] c^2 \bar{\partial}_{\mathbf{x}}^2 (a \sqrt{\kappa_*} \delta \varphi) = -\gamma \sqrt{\kappa_*} \bar{\varphi} \bar{\partial}_{\mathbf{x}}^2 \Phi - 6\gamma (\mathcal{H}' + \mathcal{H}^2) (a \sqrt{\kappa_*} \delta \varphi) - \alpha \kappa_* \Lambda^4 a^3 \left[\frac{1}{(\sqrt{\kappa_*} \varphi)^{1+\alpha}} - \frac{1}{(\sqrt{\kappa_*} \bar{\varphi})^{1+\alpha}} \right] \quad (20)$$

for the model specified by Eqs. (10, 11), where $\Phi \equiv a\phi$.

Next consider the Poisson equation, which is obtained from the Einstein equation in the weak-field and slow-motion limits. Here we use the 0-0 component of the Ricci curvature tensor, which is given as

$$R^0_0 = -3 \left(\frac{a''}{a} - \mathcal{H}^2 \right) (1 - 2\phi) + 3\psi'' + 3\mathcal{H}(\psi' + \phi') + \bar{\partial}_{\mathbf{x}}^2 \phi \quad (21)$$

using the expressions in Appendix A. According to the Einstein equations,

$$R^0_0 = \frac{\kappa_*}{2} (\rho_{\text{TOT}} + 3p_{\text{TOT}}) a^2 \quad (22)$$

where ρ_{TOT} and p_{TOT} are the total energy density and pressure, respectively. Using these two equations and subtracting the background part (which is just the Ray-

chaudhuri equation), it is straightforward to find that

$$\vec{\partial}_{\mathbf{x}}^2 \Phi = \frac{\kappa_* a^3}{2} [(\rho_{\text{TOT}} + 3p_{\text{TOT}}) - (\bar{\rho}_{\text{TOT}} + 3\bar{p}_{\text{TOT}})]. \quad (23)$$

in which we have dropped terms involving time derivatives of ψ, ϕ and $\mathcal{H}^2 \phi$, because they are much smaller than $\vec{\partial}_{\mathbf{x}}^2 \phi$ in the quasi-static limit. Using the energy-momentum tensor expressed in Eq. (4), the above equation can be rewritten as

$$\begin{aligned} & \vec{\partial}_{\mathbf{x}}^2 \Phi \\ &= \frac{\kappa_* a^3}{2} \bar{\rho}_m \left(\frac{\delta}{1+f} - \frac{1}{1+\bar{f}} \right) - \frac{\bar{f}_\varphi}{2(1+\bar{f})} c^2 \vec{\partial}_{\mathbf{x}}^2 (a\delta\varphi) \\ & \quad - \kappa_* a^3 \left[\frac{V(\varphi)}{1+f} - \frac{V(\bar{\varphi})}{1+\bar{f}} \right] \\ & \quad + a \left(\frac{1}{1+f} - \frac{1}{1+\bar{f}} \right) \left(\kappa_* \bar{\varphi}'^2 + \frac{3}{2} f'' \right) \end{aligned} \quad (24)$$

for the general Lagrangian Eq. (1) and

$$\begin{aligned} & \vec{\partial}_{\mathbf{x}}^2 \Phi \\ &= \frac{3}{2} (1 + \gamma \kappa_* \bar{\varphi}_0^2) \Omega_m H_0^2 \left[\frac{\delta}{1 + \gamma \kappa_* \varphi^2} - \frac{1}{1 + \gamma \kappa_* \bar{\varphi}^2} \right] \\ & \quad - \frac{\gamma \sqrt{\kappa_*} \bar{\varphi}}{1 + \kappa_* \bar{\varphi}^2} c^2 \vec{\partial}_{\mathbf{x}}^2 (a \sqrt{\kappa_*} \delta\varphi) \\ & \quad - \left[\frac{\kappa_* \Lambda^4 a^3}{(1 + \gamma \kappa_* \varphi^2) (\sqrt{\kappa_*} \varphi)^\alpha} - \frac{\kappa_* \Lambda^4 a^3}{(1 + \gamma \kappa_* \bar{\varphi}^2) (\sqrt{\kappa_*} \bar{\varphi})^\alpha} \right] \\ & \quad + [(1 + 3\gamma) \kappa_* \bar{\varphi}'^2 + 3\gamma \kappa_* \bar{\varphi} \bar{\varphi}''] a \\ & \quad \times \left[\frac{1}{1 + \gamma \kappa_* \varphi^2} - \frac{1}{1 + \gamma \kappa_* \bar{\varphi}^2} \right] \end{aligned} \quad (25)$$

for the model specified by Eqs. (10, 11). In these equations $\bar{\rho}_m$ is the background density for matter, $\delta \equiv \rho_m / \bar{\rho}_m$, and we have used the definition of Ω_m given in Appendix C. We have also neglected the contribution from $\delta\varphi$ to the total density and pressure, because in the quasi-static limit we have $|\delta\varphi''| \ll |\vec{\partial}_{\mathbf{x}}^2 \delta\varphi|$ and $\delta\varphi'^2 \lesssim |\bar{\varphi}' \delta\varphi'| \lesssim |\mathcal{H} \delta\varphi'| \ll \vec{\partial}_{\mathbf{x}}^2 \delta\varphi$ (which is confirmed by the N -body simulation results¹).

Finally, the equation of motion of the dark matter particles is the same as in general relativity

$$\ddot{\mathbf{x}} + 2\frac{\dot{a}}{a}\dot{\mathbf{x}} = -\frac{1}{a^3} \vec{\nabla}_{\mathbf{x}} \Phi \quad (26)$$

in which Φ is determined by the modified Poisson equation Eq. (25). The canonical momentum conjugate to \mathbf{x} is $\mathbf{p} = a^2 \dot{\mathbf{x}}$ so from the equation above we have

$$\frac{d\mathbf{x}}{dt} = \frac{\mathbf{p}}{a^2}, \quad (27)$$

$$\frac{d\mathbf{p}}{dt} = -\frac{1}{a} \vec{\nabla}_{\mathbf{x}} \Phi. \quad (28)$$

¹ According to Eq. (20) we have $\vec{\partial}_{\mathbf{x}}^2 (a \sqrt{\kappa_*} \delta\varphi) \sim \mathcal{O}(\vec{\partial}_{\mathbf{x}}^2 \Phi)$, implying that $a \sqrt{\kappa_*} \delta\varphi \sim \mathcal{O}(\Phi)$, so neglecting time derivatives of $\delta\varphi$ is just like dropping time derivatives of ψ and ϕ , which we have already done to obtain the modified Poisson equation.

Eqs. (20, 25, 27, 28) will be used in the code to evaluate the forces on the dark-matter particles and evolve their positions and momenta in time. But before applying them to the code we still need to switch to code units (see Sect. 2.3), further simplify them and create the discrete version (see Appendix B).

2.3. Code Units

In our numerical simulation we use a modified version of MLAPM ((Knebe, Green & Binney 2001)), and we will have to change or add our Eqs. (20, 25, 27, 28) to it. The first step is to convert the quantities to the code units of MLAPM. Here, we briefly summarise the main results.

The (modified) MLAPM code uses the following internal units (where a subscript c stands for "code"):

$$\begin{aligned} \mathbf{x}_c &= \mathbf{x}/B, \\ \mathbf{p}_c &= \mathbf{p}/(H_0 B) \\ t_c &= t H_0 \\ \Phi_c &= \Phi/(H_0 B)^2 \\ \rho_c &= \rho/\bar{\rho}, \\ u &= a c^2 \sqrt{\kappa} \delta\varphi / (H_0 B)^2, \end{aligned} \quad (29)$$

where B denotes the comoving size of the simulation box, H_0 is the present Hubble constant, and ρ is the matter density. In the last line the quantity u is the scalar field perturbation $\delta\varphi$ expressed in terms of code units and is new to the MLAPM code.

In terms of u , as well as the (dimensionless) background value of the scalar field, $\sqrt{\kappa} \bar{\varphi}$, some relevant quantities are expressed in full as

$$\begin{aligned} V(\varphi) &= \frac{\Lambda^4}{\left(\sqrt{\kappa} \bar{\varphi} + \frac{B^2 H_0^2}{a c^2} u \right)^\alpha}, \\ f(\varphi) &= 1 + \gamma \left(\sqrt{\kappa} \bar{\varphi} + \frac{B^2 H_0^2}{a c^2} u \right)^2, \\ V_\varphi(\varphi) &= -\alpha \frac{\sqrt{\kappa} \Lambda^4}{\left(\sqrt{\kappa} \bar{\varphi} + \frac{B^2 H_0^2}{a c^2} u \right)^{1+\alpha}}, \\ f_\varphi(\varphi) &= 2\gamma \sqrt{\kappa} \left(\sqrt{\kappa} \bar{\varphi} + \frac{B^2 H_0^2}{a c^2} u \right), \end{aligned} \quad (30)$$

and the background counterparts of these quantities can be obtained simply by setting $u = 0$ (recall that u represents the perturbed part of the scalar field) in the above equations.

We also define

$$\lambda \equiv \frac{\kappa \Lambda^4}{3 H_0^2}, \quad (31)$$

which will be used frequently below.

Making discrete versions of the above equations for N -body simulations is then straightforward, and we refer the interested readers to Appendix B to the whole treatment, with which we can now proceed to do N -body simulations.

3. SIMULATION DETAILS

3.1. The N -Body Code

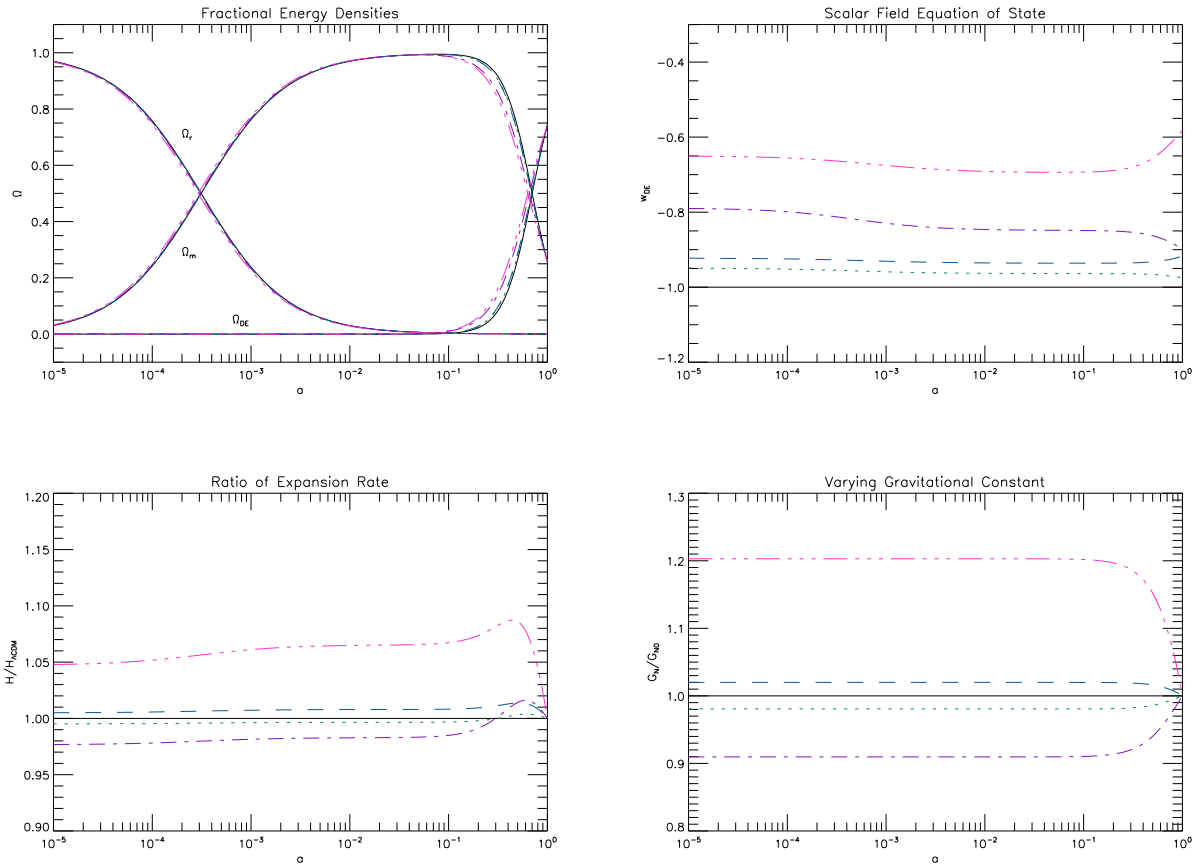


FIG. 1.— (Color Online) The background evolution in the extended quintessence models. *Upper-left panel*: the fractional energy densities for matter (Ω_m), radiation (Ω_r) and the scalar field dark energy (Ω_{DE}), as indicated besides the curves, as functions of the scale factor a ($a_0 = 1$ today). *Upper-right panel*: the scalar field equation of state $w = p_{\text{DE}}/\rho_{\text{DE}}$ as a function of a . *Lower-left panel*: the ratio between the Hubble expansion rates of the extended quintessence model and Λ CDM as a function of a . *Lower-right panel*: the a -evolution of the effective gravitational constant that governs the growth of matter density perturbations ($G_{\text{N}0}$ is its value today). In all panels the black solid, green dot, blue dashed, purple dot-dashed, pink dot-dot-dashed curves represent respectively the results for Λ CDM and extended quintessence models with $(\alpha, \gamma) = (0.1, -0.2)$, $(0.1, 0.2)$, $(0.5, -0.2)$, $(0.5, 0.2)$.

Some of our main modifications to the MLAPM code for the coupled scalar field model are:

1. We have added a solver for the scalar field, based on Eq. (B7). It uses a nonlinear Gauss-Seidel scheme for the relaxation iteration and the same criterion for convergence as the default Poisson solver. But it adopts a V-cycle instead of the self-adaptive scheme in arranging the Gauss-Seidel iterations.
2. The value of u solved in this way is then used to calculate the total matter density, which completes the calculation of the source term for the Poisson equation. The latter is then solved using a fast Fourier transform on the domain grids and self-adaptive Gauss-Seidel iteration on refinements.
3. The gravitational potential Φ obtained in this way is then used to compute the force, which is used to displace and kick the particles.

There are a lot of additions and modifications to ensure smooth interface and the newly added data structures. For the output, as there are multilevel grids all of which host particles, the composite grid is inhomogeneous and so we choose to output the positions and momenta of the particles, plus the gravity and values of Φ and u at the positions of these particles. We also output the potential and scalar field values on the 128^3 domain grid.

3.2. Physical and Simulation Parameters

The physical parameters we use in the simulations are as follows: the present-day dark-energy fractional energy density $\Omega_{\text{DE}} = 0.743$ and $\Omega_m = \Omega_{\text{CDM}} + \Omega_{\text{B}} = 0.257$, $H_0 = 71.9 \text{ km/s/Mpc}$, $n_s = 0.963$, $\sigma_8 = 0.769$. Our simulation box has a size of $64h^{-1} \text{ Mpc}$, where $h = H_0/(100 \text{ km/s/Mpc})$. We simulate four models, with parameters $(\alpha, \gamma) = (0.1, -0.2)$, $(0.1, 0.2)$, $(0.5, -0.2)$ and $(0.5, 0.2)$ respectively. In all those simulations, the mass resolution is $1.114 \times 10^9 h^{-1} M_{\odot}$; the particle number is 256^3 ; the domain grid is a $128 \times 128 \times 128$ cubic and the

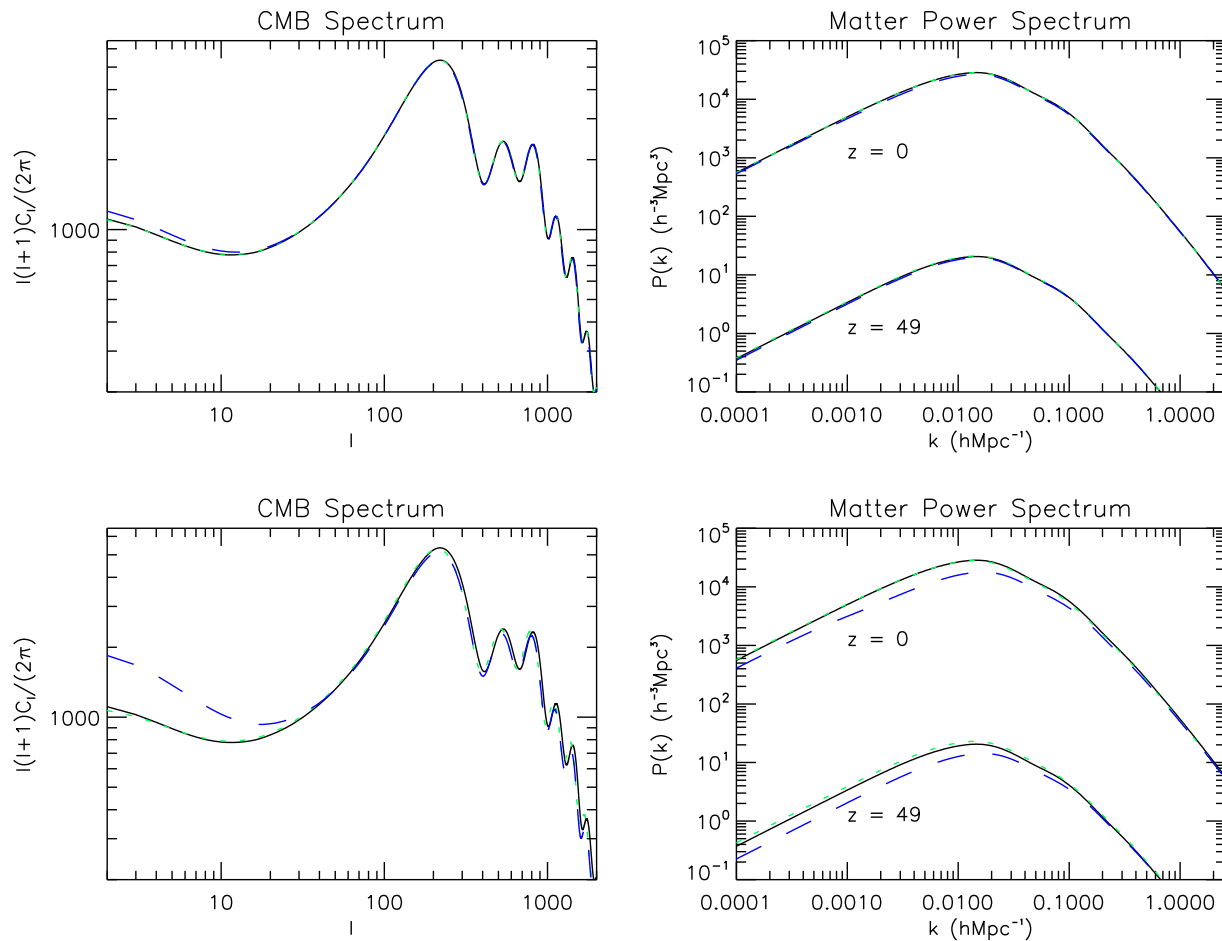


FIG. 2.— (Color Online) The CMB (*left panels*) and matter power spectra (*right panels*) for the extended quintessence models compared with those of the Λ CDM. The upper panels are for the models with $\alpha = 0.1$ while the lower panels are for those with $\alpha = 0.5$. The black solid, green dotted and blue dashed curves represent respectively the curves for Λ CDM and extended quintessence with $\gamma = -0.2$ and $\gamma = 0.2$. For the matter power spectra, we plot the results for two different output redshifts, $z = 0$ and 49, as indicated below the curves.

finest refined grids have 16384 cells on each side, corresponding to a force resolution of about $12h^{-1}$ kpc.

We also run a Λ CDM simulation with the same physical parameters and initial condition (see below).

3.3. Background and Linear Perturbation Evolution

Since the coupling between the scalar field and the curvature produces a time-varying effective gravitational constant, and the scalar field contributes to the total energy-momentum tensor, we expect that cosmology in the extended quintessence models is generally different from Λ CDM at the background and linear perturbation levels. A good understanding of this will be helpful in our analysis of the results from N -body simulations, and this is the subject of this subsection.

Our algorithm and formulae for the background cosmology are detailed in Appendix C, and are implemented in MAPLE. We output the relevant quantities in a predefined time grid, which could be used (via interpolation) in the linear perturbation and N -body computations.

Fig. 1 shows the time evolutions of some background quantities of interests. For ease of comparison we have

chosen Ω_m and Ω_r to be the same in all models including the Λ CDM one (for definitions of Ω_m and Ω_r see Appendix C), and as a result in the upper left panel the curves for different models converge at common right-hand ends. We see increasing α results in an earlier and slower growth of Ω_{DE} ($\Omega_{\text{DE}} = 1 - \Omega_m - \Omega_r$). This indicates a larger dark energy equation of state parameter, w , which is confirmed by the upper right panel. Physically, this is because, the larger α is, the steeper the potential becomes and thus the faster the scalar field rolls. Notice that w is also larger for positive γ , with α being the same. This is because in Eq. (6) the Ricci scalar $R < 0$ and for positive γ the term $\frac{R}{2\kappa_*} f_\varphi$ has the same sign as V_φ , thus helping the scalar field to roll faster. Because of its large predicted value of w , the model $(\alpha, \gamma) = (0.5, 0.2)$ is already excluded by cosmological data, but here we shall keep it for purely theoretical interest (*i.e.*, to see how changing α or γ changes the nonlinear structure formation).

We are also interested in how the expansion rate in an extended quintessence model differs from that in Λ CDM,

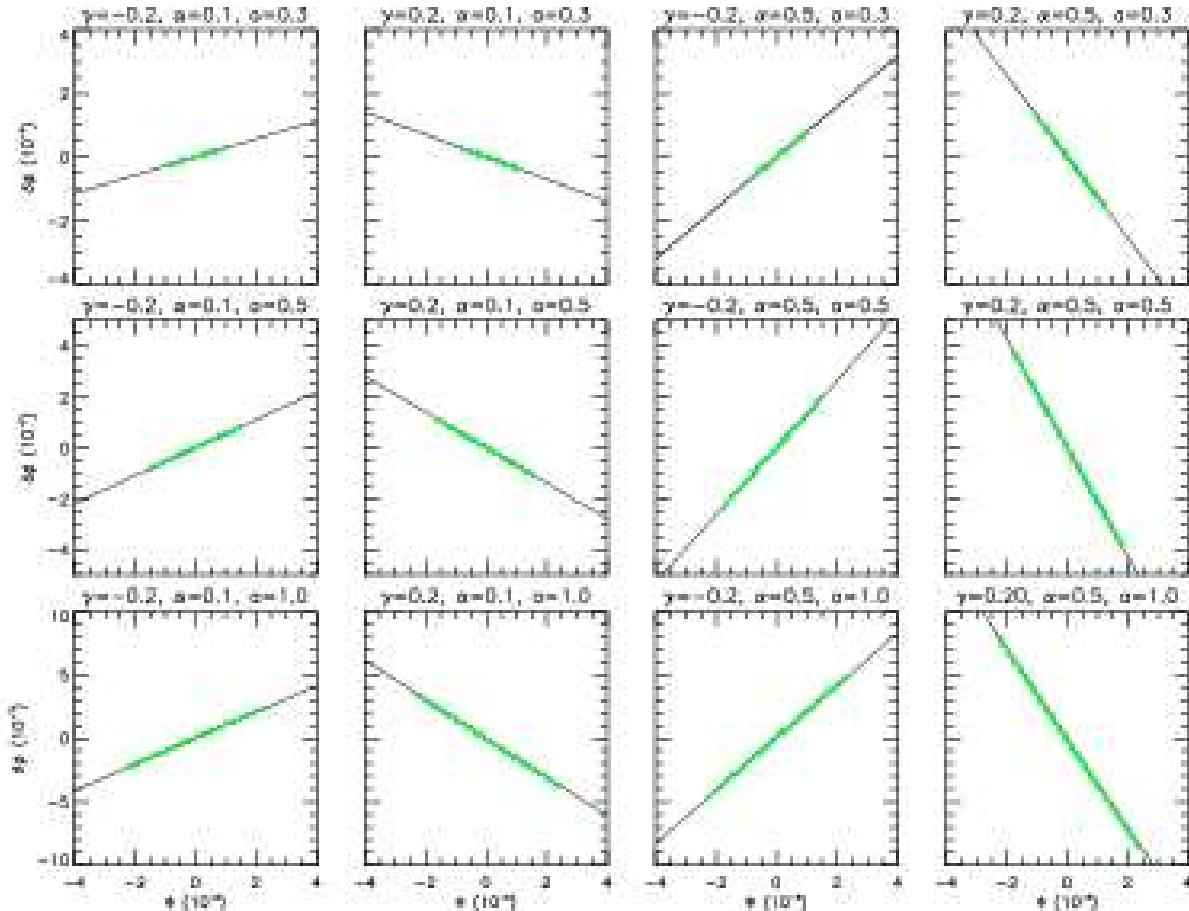


FIG. 3.— (Color Online) The relation between the magnitudes of the scalar field perturbation $a\sqrt{\kappa_*}\delta\varphi$ (in unit of 10^{-7}) and gravitational potential Φ (in unit of 10^{-6}) for the four extended quintessence models (the four columns) at three different output times $a = 0.3, 0.5, 1.0$ (the three rows) as indicated above the frames. The black solid line in each panel represents the analytical approximation Eq. (35) (see text) and the $\sim 10,000$ green dots the results from a thin slice of our simulation boxes.

and the results for our models are shown in the lower-left panel of Fig. 1, which plots the $H/H_{\Lambda\text{CDM}}$ as a function of a . The rather odd behaviour of the models at low redshift is because of the complicated evolution of the scalar field (and the fact that we have chosen H_0 to be the same for all models, again for ease of comparison), while the high-redshift behaviour could be seen directly from Eq. (C4). In Eq. (C4) the energy density of the scalar field can be dropped at high z , and so we have

$$\left(\frac{\mathcal{H}}{\mathcal{H}_0}\right)^2 \approx \frac{1+f_0}{1+f} \Omega_m a^{-1} \quad (32)$$

where we have also neglected the radiation for simplicity (which is valid after the matter-radiation equality). This shows that in extended quintessence models the gravitational constant relevant for the background cosmology is rescaled by $(1+f_0)/(1+f)$. Because $f_0 = f(\varphi_0)$ where φ_0 is the present-day value of φ , and φ is monotonically increasing in time, so for our choice of $f(\varphi)$ [cf. Eq. (11)] we have $(1+f_0)/(1+f) > 1$ for $\gamma > 0$ and $(1+f_0)/(1+f) < 1$ for $\gamma < 0$: thus models with $\gamma > 0$ have $H/H_{\Lambda\text{CDM}} > 1$.

It turns out that the gravitational constant relevant for the growth of matter density perturbations is also differ-

ent from the one governing the background cosmology. If we denote the matter density perturbation by δ_m , then it can be shown, using the linear perturbation equations, that on small scales the evolution equation for δ_m reduces to

$$\delta_m'' + \mathcal{H}\delta_m' = G_N \frac{3\mathcal{H}_0^2}{2} \Omega_m \delta_m a^2 \quad (33)$$

in which $' \equiv d/d\tau$ and τ is the conformal time (see Appendix C), and we have defined

$$G_N \equiv \frac{1+f_0}{1+f} \frac{2+2f+4\left(\frac{df}{d\sqrt{\kappa_*}\varphi}\right)^2}{2+2f+3\left(\frac{df}{d\sqrt{\kappa_*}\varphi}\right)^2}. \quad (34)$$

Note that this quantity could also be directly read off from the modified Poisson equation Eq. (B3).

In the lower right panel of Fig. 1 we display the evolution for G_N in the models considered. Again, G_N is larger at earlier times for positive γ and smaller for negative γ , because of our specific choice of $f(\varphi)$ in Eq. (11), and the fact that φ is always increasing in time.

It is well known that a higher rate of background ex-

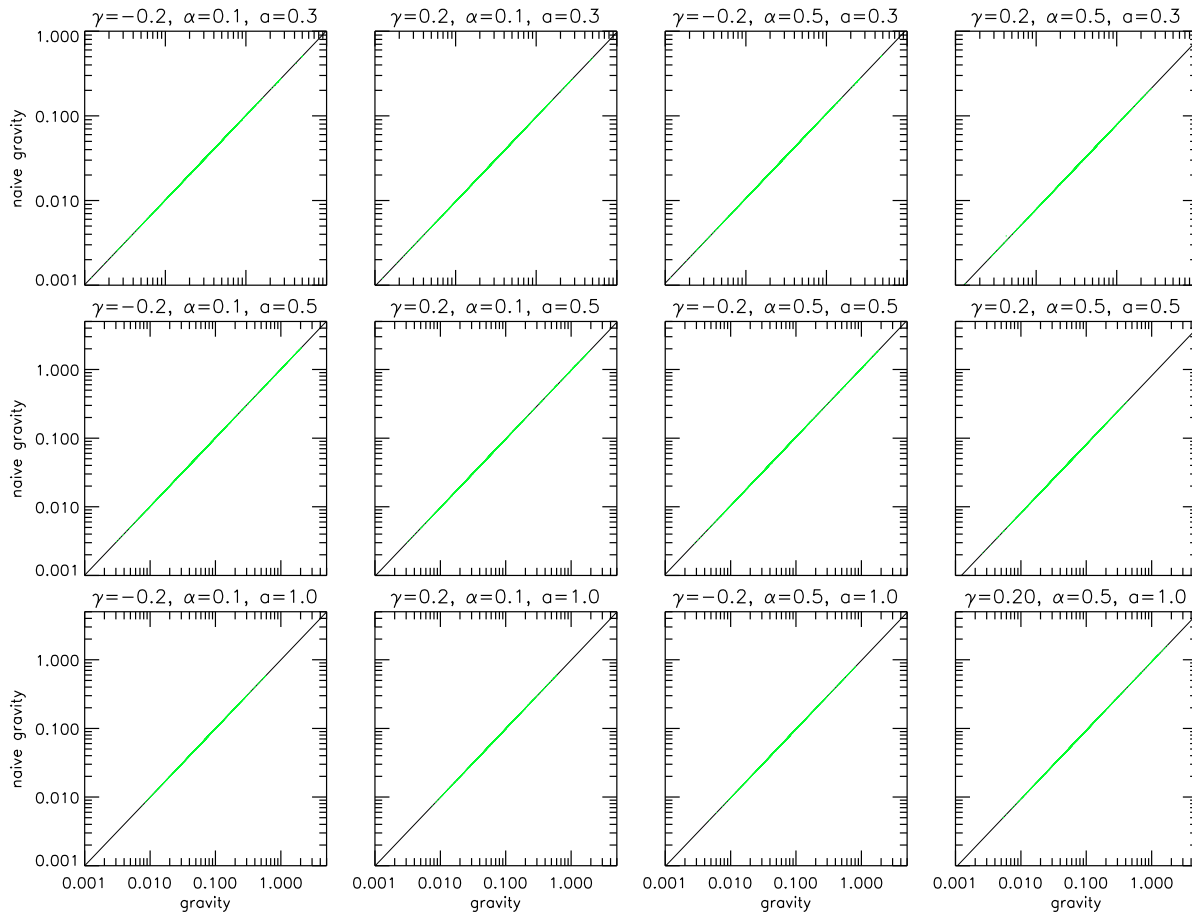


FIG. 4.— (Color Online) The relation between the magnitudes of the naïve gravity (see text) and full gravity for the four extended quintessence models (the four columns) at three different output times $a = 0.3, 0.5, 1.0$ (the three rows) as indicated above the frames. The black solid line in each panel represents the analytical approximation Eq. (34) (see text) and the $\sim 10,000$ green dots the results from the simulations.

pansion means that structures have less time to form, and a larger G_N speeds up the structure formation. These two effects therefore cancel each other to some extent, which results in a weaker net effect of an extended quintessence field on the large scale structure formation. This is confirmed by our linear perturbation computation depicted in Fig. 2. In the right-hand panels of this figure we have plotted the matter power spectra for different models at two different redshifts (0 and 49). It is interesting to note that on small scales the matter power is closer to that of Λ CDM, despite the significant differences in background expansion rate and G_N (cf. Fig. 1). Because of this, we shall choose Λ CDM initial condition for our N -body simulations for all our models, saving the effort of generating separate initial conditions for different models.

The left hand panels of Fig. 2 display the CMB power spectra for the models we consider. Again the difference from Λ CDM is fairly small, and there is only a small shift of the CMB peaks even though the background expansion rate changes quite a bit. The latter is because peak positions are determined by the ratio of the sound horizon size at decoupling and the angular distance to the decoupling, and in our model both of these decrease/increase as the Universe expands faster/more slowly, their ratio does not change much.

To briefly summarise, the study of background cosmology and linear perturbation shows that a modified back-

ground expansion rate and a rescaled gravitational constant, the two most important factors affecting structure formation in extended quintessence models are opposite effects. It is then of interest to see how these two effects compete in the nonlinear regime.

4. N -BODY SIMULATION RESULTS

This section lists the results of extended quintessence N -body simulations. We shall start with a few preliminary results which both give some basic idea about the extended quintessence effects and serve as a cross check of our codes. Then we discuss the key observables for the nonlinear structure formation such as matter power spectrum, mass function and halo properties. We also comment on the halo profile of the scalar field and the spatial variation of gravitational constant.

4.1. Preliminary Results

As mentioned above, in both the linear and N -body codes we compute background quantities via an interpolation of some pre-computed table. Because background cosmology is important in determining the structure formation, it is important to check its accuracy. For this we have recorded in Table 1 The age of the universe today for different models as computed by these two codes. The two codes are compatible with each other indeed.

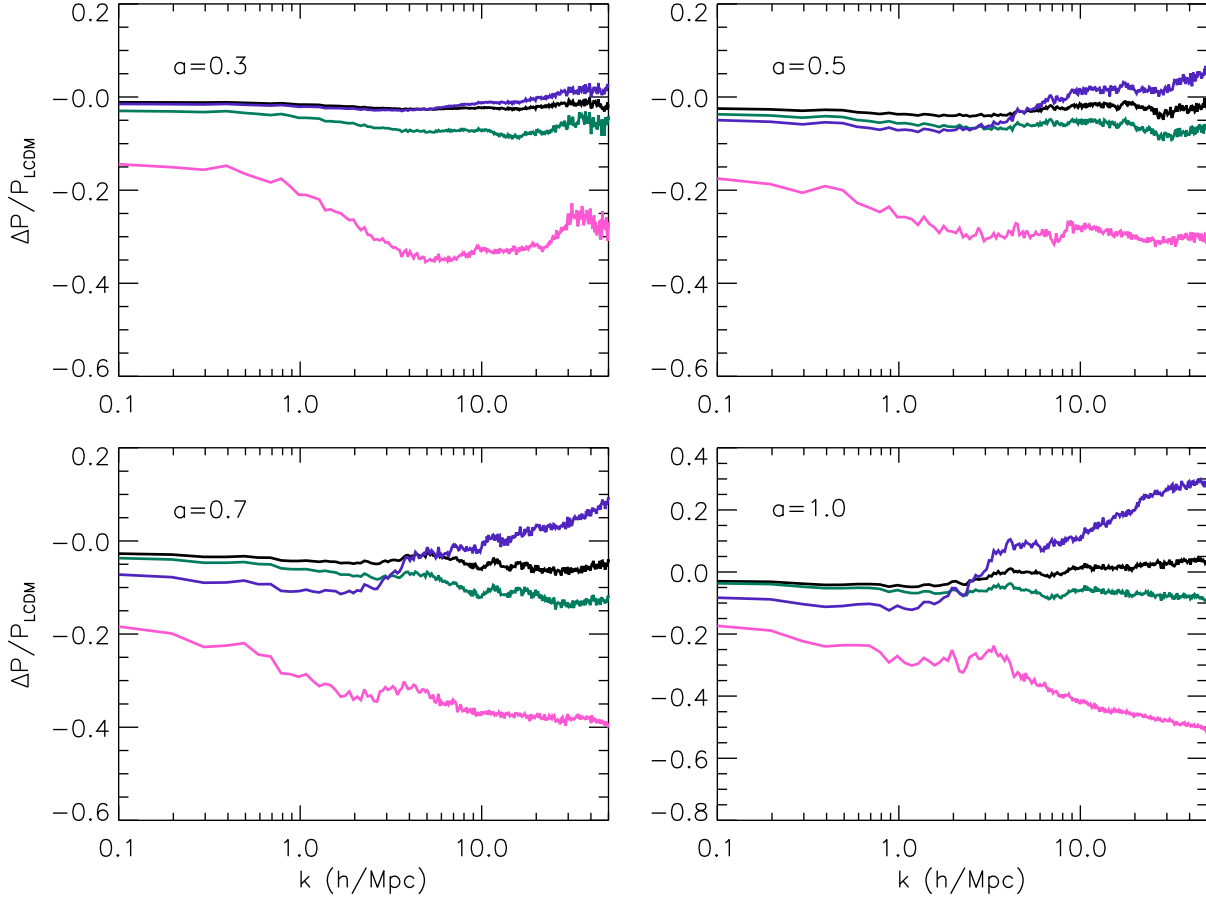


FIG. 5.— (Color Online) The fractional difference between the nonlinear power spectra for the extended quintessential and Λ CDM models. The results for the four models of $(\alpha, \gamma) = (0.1, -0.2), (0.1, 0.2), (0.5, -0.2)$ and $(0.5, 0.2)$ are respectively represented by the black, green, purple and pink curves. The four panels are for four output times $\alpha = 0.3, 0.5, 0.7$ and 1.0 as indicated inside the corresponding frames.

TABLE 1
CURRENT AGE OF THE UNIVERSE FOR THE DIFFERENT MODELS
UNDER CONSIDERATION AS COMPUTED BY THE LINEAR
PERTURBATION AND N -BODY CODES. UNIT IS GYR.

model	linear code	N -body code
Λ CDM	13.680	13.678
$(\alpha, \gamma) = (0.1, -0.2)$	13.639	13.638
$(\alpha, \gamma) = (0.1, 0.2)$	13.408	13.408
$(\alpha, \gamma) = (0.5, -0.2)$	13.513	13.513
$(\alpha, \gamma) = (0.5, 0.2)$	12.097	12.096

Because one of the advantages of our N -body code is that it solves the scalar field perturbation explicitly, it is important to check that the solution is with expectations. From Eqs. (B1, B2) it could be seen clearly that, if the contribution to the local density and pressure from the scalar field is negligible compared with that from matter, then the modified Poisson equation and scalar field equation of motion end up with the same source term (up to

a $\bar{\varphi}$ -dependent coefficient). In this situation we expect

$$u = -\frac{2\gamma\sqrt{\kappa_*}\bar{\varphi}}{1 + \frac{8\gamma^2\kappa_*\bar{\varphi}^2}{1+\gamma\kappa_*\bar{\varphi}^2}}\Phi_c, \quad (35)$$

which means that u is simply proportional to Φ_c with a time-dependent coefficient. In Fig. 3 we have checked this relation explicitly: we select a thin slice of the simulation box, fetch the values for u and Φ_c at the positions of the particles (about 10000 in total) therein, and display them as scatter plots. The solid curve is the approximation Eq. (35) while the green dots are simulation results; we can see they agree very well with each other, showing that the above approximation is a good one. Note that the scalar field perturbation $a\sqrt{\kappa_*}\delta\varphi$ is generally less than 10^{-6} , compared with the background value $\sqrt{\kappa_*}\bar{\varphi} \sim \mathcal{O}(0.1-1)$. This confirms that it is consistent to neglect the perturbation in scalar field density/pressure, drop terms such as $\delta\varphi$ and $\delta\dot{\varphi}$, and replace φ by $\bar{\varphi}$ in coefficients of perturbation quantities such as $\bar{\partial}_x^2(a\sqrt{\kappa_*}\delta\varphi)$ and $\bar{\partial}_x^2\Phi$. It also serves as a check of the numerical code.

As a final consistency check, let us consider the total gravitational force on particles. In extended quintessence

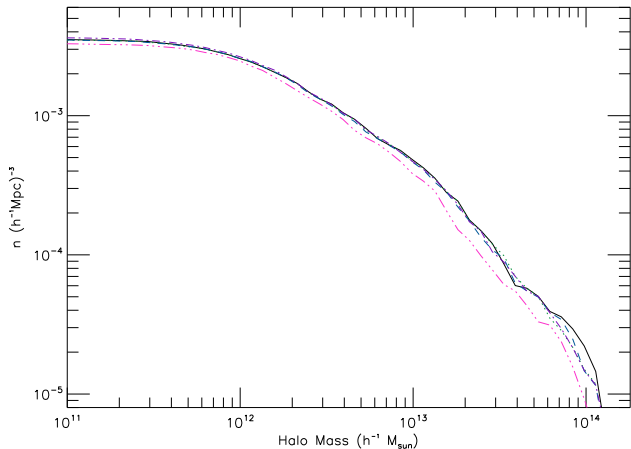


FIG. 6.— (Color Online) The mass functions for the models considered. The black solid, green-dotted, blue-dashed, purple dot-dashed and pink dot-dot-dot-dashed curves stand for the results for Λ CDM and extended quintessence models with $(\alpha, \gamma) = (0.1, -0.2)$, $(0.1, 0.2)$, $(0.5, -0.2)$ and $(0.5, 0.2)$ respectively. The horizontal axis denotes the halo mass (in unit of $h^{-1}M_{\odot}$) and the vertical axis is the halo number density (in unit of $h^3\text{Mpc}^{-3}$). Only the results at $a = 1$ are plotted.

models, this is given by Eq. (B2), and when the perturbation in the scalar field density/pressure is negligible (which is the case as shown above) we get

$$\nabla^2\Phi_c \approx \frac{3}{2}G_N\Omega_m H_0^2(\rho_c - 1) \quad (36)$$

in which G_N is given in Eq. (34). On the other hand, if we consider (naïvely) that gravity is described by general relativity, then we should neglect the G_N on the right-hand side. Manipulating Eqs. (B1, B2) we obtain:

$$\frac{1 + \gamma\kappa_*\bar{\varphi}_0^2}{1 + \gamma\kappa_*\bar{\varphi}^2} \nabla^2 \left(\Phi_c + \frac{\gamma\sqrt{\kappa_*}\bar{\varphi}}{1 + \gamma\kappa_*\bar{\varphi}^2} u \right) \approx \frac{3}{2}\Omega_m H_0^2(\rho_c - 1).$$

Thus $\frac{1 + \gamma\kappa_*\bar{\varphi}_0^2}{1 + \gamma\kappa_*\bar{\varphi}^2} \left(\Phi_c + \frac{\gamma\sqrt{\kappa_*}\bar{\varphi}}{1 + \gamma\kappa_*\bar{\varphi}^2} u \right)$ acts as the potential for naïve gravity (*i.e.*, general relativity), and by differencing it we could obtain the naïve gravitational force. In Fig. 4 we show the scatter plot of the naïve gravity versus full gravity for the same particles as in Fig. 3 (green dots) as well as their approximate ratio G_N (solid line). Again, the agreement is remarkably good.

4.2. Nonlinear Matter Power Spectrum

As we have seen above, the linear matter power spectrum for the extended quintessence model really does not show much useful information on small scales, and so we need to investigate whether nonlinear effects could change this situation and therefore potentially place more meaningful constraints.

Fig. 5 provides a positive answer to this question. Here we have plotted the fractional difference of the extended quintessential nonlinear matter power spectrum from that for Λ CDM (remember that we use the same initial condition for all simulations). We can see that for the models with $\alpha = 0.1$ the differences are small even in the nonlinear regime, indicating that the scalar field really does not affect the matter distribution significantly if the potential is flat. However, for the $\alpha = 0.5$ cases

in which the coupling strength γ remains the same, the difference could be as large as 30% \sim 50%, guaranteeing an observable signature.

Furthermore, for negative γ (the purple curve) the extended quintessential power spectrum beats the Λ CDM one on small scales, whereas for the positive γ case (the pink curve) it is just the opposite. As shown before, when $\gamma < 0$, both the background expansion rate and the effective gravitational constant governing the structure formation decrease, boosting and weakening the collapse of matter respectively. In our $\alpha = 0.5$ cases the first effect has clearly taken over on small scales.

4.3. Mass Function

A second important observable is the mass function. This gives the number density of dark matter halos as a function of halo mass. For this we need to identify the dark matter halos from the output particle distribution of the N -body simulations, and this determination is performed using a modified version of MHF (Knebe & Gibson 2004), MLAPM’s default halo finder.

MHF optimally utilizes the refinement structure of the simulation grids to pin down the regions in which potential halos reside and organize the refinement hierarchy into a tree structure. MLAPM refines grids according to the particle density on them and so the boundaries of the refinements are simply isodensity contours. MHF collects the particles within these isodensity contours (as well as some particles outside). It then performs the following operations: (i) assuming spherical symmetry of the halo, calculate the escape velocity v_{esc} at the position of each particle, (ii) if the velocity of the particle exceeds v_{esc} then it does not belong to the virialized halo and is removed. Steps (i) and (ii) are then iterated until all unbound particles are removed from the halo or the number of particles in the halo falls below a pre-defined threshold, which is 20 in our simulations. Note that the removal of unbound particles is not used in some halo finders using the spherical overdensity (SO) algorithm, which includes the particles in the halo as long as they are within the radius of a virial density contrast. Another advantage of MHF is that it does not require a predefined linking length in finding halos, such as the friend-of-friend procedure.

Our modification to MHF is simple: because the effective gravitational constant in the extended quintessence models is rescaled by a factor G_N [cf. Eq. (34)], the escape velocity of particles from a halo is also multiplied by this factor, and in MHF we have only changed the criterion for removing particles from virialised halos accordingly. In reality, because we are only interested in the $a = 1$ halos in this work, G_N is quite close to 1 and the effect of our modification is not large.

The mass functions for our simulated models are shown in Fig. 6. It shows that all extended quintessence models considered here, irrespective of their parameters, produce less massive halos than Λ CDM, whereas (only) the model $(\alpha, \gamma) = (0.5, -0.2)$ produces a larger number of less massive halos. These features are in broad agreement with those shown in the matter power spectra (Fig. 5) where all models show less matter clustering on the large scales, whereas (only) the model $(\alpha, \gamma) = (0.5, -0.2)$ shows more power on small scales. The physical reason is again the competition between the modified background expansion rate and rescaled effective gravitational constant G_N .

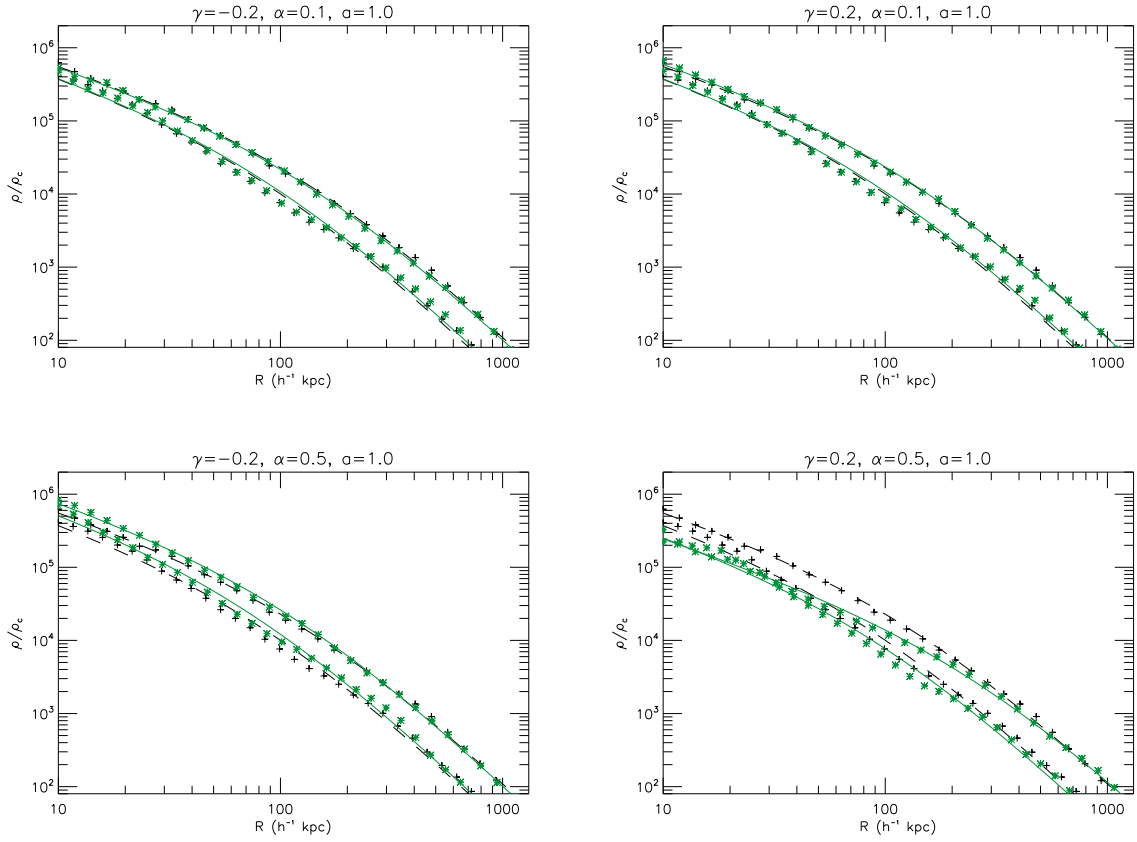


FIG. 7.— (Color Online) The NFW fitting results for two halos randomly selected from the 80 most massive halos in each simulation (see text for details). The upper and lower green asterisks represent respectively the density profile from N -body simulation for the more and less massive halo, and the green solid curves their NFW fittings. For comparison we also shown the corresponding N -body (black crosses) and fitting (black dashed curves) results for the Λ CDM model. The horizontal axis is the distance from halo centre (in units of h^{-1} kpc) and the vertical axis is the density contrast. The four panels are for the four models as indicated above the frames.

4.4. Halo Properties

In the Λ CDM paradigm, it is well known that the internal density profiles of dark matter halos are very well described by the Navarro-Frenk-White (Navarro, Frenk & White 1996) formalism

$$\frac{\rho(r)}{\rho_c} = \frac{\beta}{\frac{r}{R_s} \left(1 + \frac{r}{R_s}\right)^2} \quad (37)$$

where ρ_c is the critical density for matter, β is a dimensionless fitting parameter and R_s a second fitting parameter with length dimension. β and R_s are generally different for different halos and should be fitted for individual halos, but the formula Eq. (37) is quite universal.

We are thus interested in whether the halo profiles in an extended quintessential Universe are also featured by this universal form. For this we select the 80 most massive halos from each simulation and fit their density profiles to Eq. (37). The results show that the NFW profile describes the extended quintessential halos at least as well as it does for the Λ CDM halos. Fig. 7 shows the fittings for two halos randomly picked out of the 80: one at $\sim (10.34, 28.63, 13.91)h^{-1}$ Mpc with mass $\sim 1.88 \times 10^{14}M_\odot$

and the other at $(41.77, 31.91, 21.20)h^{-1}$ Mpc with a mass $\sim 4.98 \times 10^{13}M_\odot$.

There are some interesting features in Fig. 7. Firstly, for the models with $\alpha = 0.1$ (the top panels) the halo density profile for extended quintessence models (green asterisks) is very similar to the Λ CDM results (black crosses) and thus their fittings almost coincide. Secondly, for the model of $(\alpha, \gamma) = (0.5, -0.2)$, the chosen halos show more concentration of the density profiles in the scalar model than in Λ CDM. Thirdly, the model of $(\alpha, \gamma) = (0.5, -0.2)$ has just the opposite trend and suffers a suppression of density in large parts of chosen halos.

To verify that the above features are actually typical for the corresponding models, we have plotted in Fig. 8 the fitting results for all the 80 massive halos in all simulated models. Here in addition to the NFW concentration parameter $c_{\text{NFW}} = r_{200}/R_s$, where r_{200} is the radius at which the density is equal to 200 times the critical density ρ_c and R_s the NFW parameter, we have also shown the fitting errors for each halo.

We would like to point out several important implications of Fig. 8. Firstly, for all models the fitting error for the extended quintessential halos (lower green asterisks)

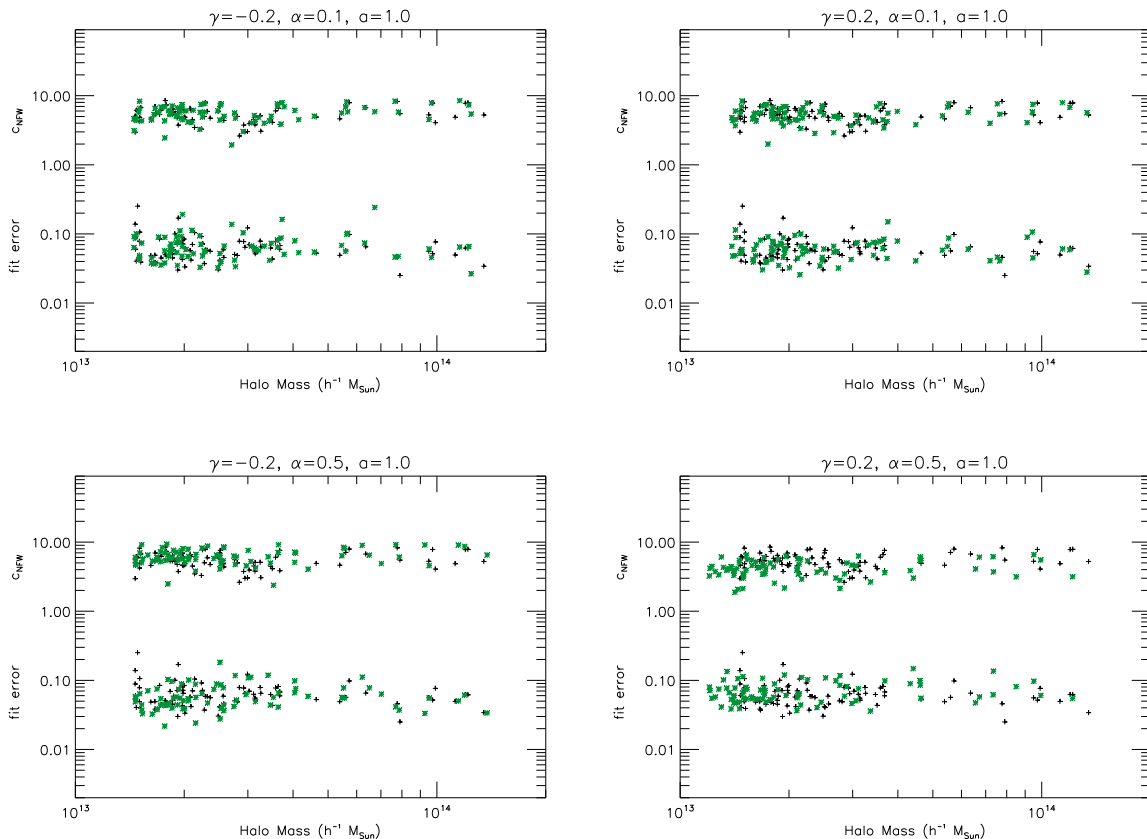


FIG. 8.— (Color Online) Scatter plot of the NFW fitting of the dark matter halo density profiles for the 80 most massive halos in each simulation box. In all panels the black crosses and green asterisks stand for results of Λ CDM and extended quintessence models respectively. The upper cluster of points in each panel represents the fitted c_{NFW} and the lower cluster is for the fitting error, as indicated beside the vertical axis. The horizontal axis is the halo mass (in units of $h^{-1}M_{\odot}$). The four panels are for the models as indicated above the frames.

isks) is comparable to that for the Λ CDM halos (lower black crosses), indicating that the density profiles for the former are equally well described by the NFW formula Eq. (37). Secondly, for the models with $\alpha = 0.1$ (the top panels) we can see that the fitted c_{NFW} for the extended quintessential halos is comparable to that for Λ CDM, which is in agreement with our finding in Fig. 7 that the density profiles for the chosen halos are almost the same as in the Λ CDM prediction. Thirdly, for the model of $(\alpha, \gamma) = (0.5, -0.2)$, the halos tend to be *more* concentrated (*i.e.*, with *larger* c_{NFW}) than in Λ CDM. Fourthly, for the model $(\alpha, \gamma) = (0.5, 0.2)$, the halos tend to be *less* concentrated (*i.e.*, with *smaller* c_{NFW}) than in Λ CDM. The above three features show that our qualitative findings in Fig. 7 are quite typical. Finally, the halo masses in the model of $(\alpha, \gamma) = (0.5, -0.2)$ are on average smaller than those in Λ CDM, because the upper green asterisks in the lower right panel consistently shift leftwards with respect to the upper black crosses: this is consistent with the mass function result that this model produces less massive halos than Λ CDM.

In summary, the halo density profiles for the extended quintessence models are well described by the NFW formula, but the existence of the scalar field and in particu-

lar its coupling to curvature do change the concentration parameters of the halos, so long as the potential is not too flat. It seems that the modified background expansion rate beats the effect of the rescaled effective gravitational constant here.

4.5. Halo Profile for Scalar Field Perturbation

We have already seen that the coupling between the scalar field and the curvature scalar causes time and spatial variations of the locally measured gravitational constant κ_{\oplus} . It is then of our interest to ask how κ_{\oplus} varies across a given halo and whether this could produce observable effects. This subsection answers this question, by giving an analytical formula and comparing it with numerical results.

Recall that Fig. 3 shows that to a high precision the scalar field perturbation $a\sqrt{\kappa_*}\delta\varphi$ is proportional to the gravitational potential Φ [cf. Eq. (35)] everywhere. This means that if we could derive an analytical formula for Φ in halos, then we know $a\sqrt{\kappa_*}\delta\varphi$ straightforwardly. Such a derivation has been done in (Li, Mota & Barrow 2010) for a different model, but here we shall briefly repeat it for the extended quintessence model for completeness.

Assuming Eq. (37) as the density profile and sphericity

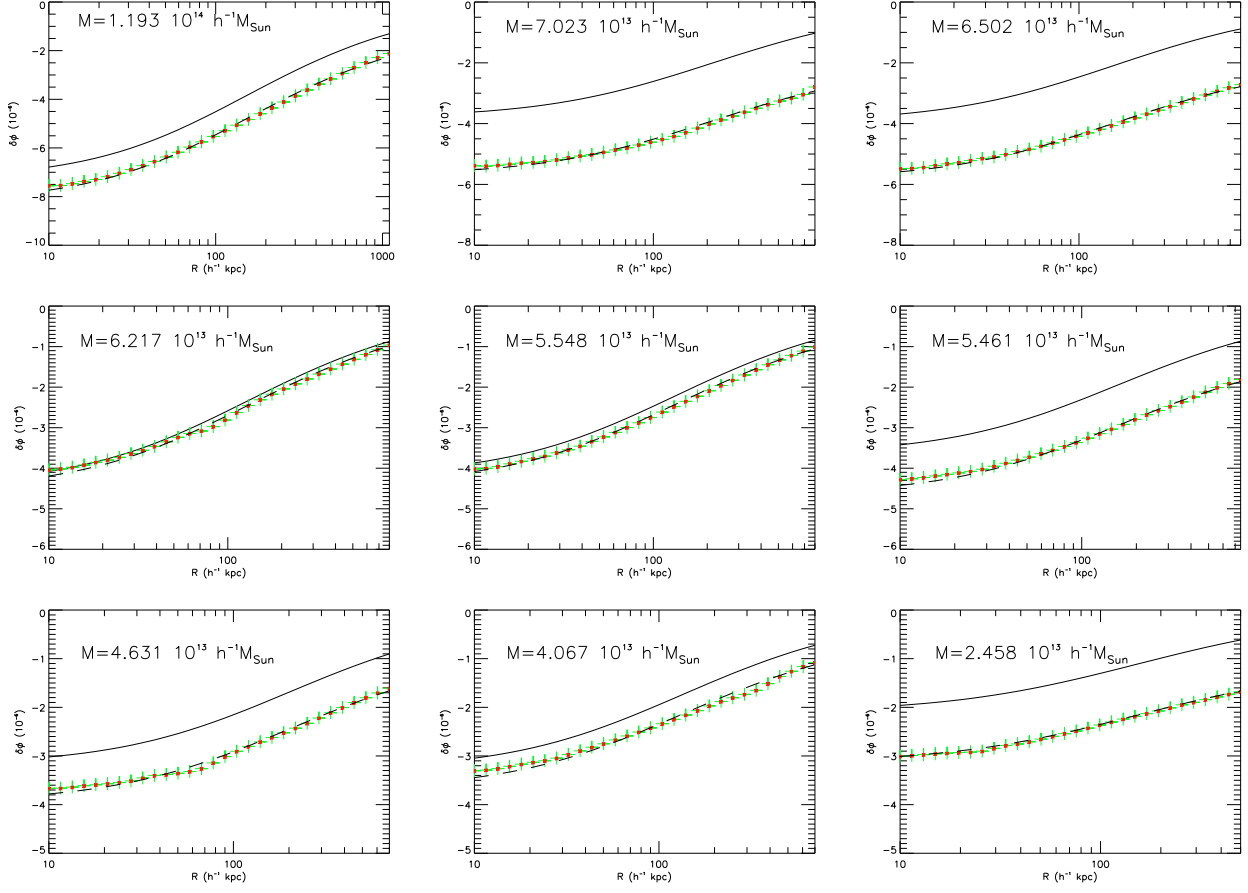


FIG. 9.— (Color Online) Comparison between our analytic formula for the scalar field perturbation $a\sqrt{\kappa_*}\delta\varphi$ [Eq. (43)] and the results from numerical simulation. The nine panels are for nine halos selected from the simulation box, whose masses are indicated inside each frame. In each panel the solid curve is Eq. (43) with $\Phi_* = 0$, green crosses are the numerical results for $a\sqrt{\kappa_*}\delta\varphi$, the dashed line is Eq. (43) with Φ_* appropriately tuned to match the green crosses, and the red asterisks are the $a\sqrt{\kappa_*}\delta\varphi$ computed from the value of Φ using Eq. (35). The horizontal axis is the distance from the halo centre, and vertical axis stands for the value of $a\sqrt{\kappa_*}\delta\varphi$.

of halos, we can derive $V_c(r)$, the circular velocity of a particle moving around the halo at a distance r from halo centre, to be

$$V_c^2(r) = \frac{GM(r)}{r} = 4\pi G\beta\rho_c R_s^3 \left[\frac{1}{r} \ln\left(1 + \frac{r}{R_s}\right) - \frac{1}{R_s + r} \right] \quad (38)$$

where $M(r)$ is the mass enclosed in radius r , G is the *properly rescaled* gravitational constant. Again, this equation is parameterized by β and R_s . From a simulation point of view, it is straightforward to measure $M(r)$ and then use Eq. (38), instead of Eq. (37), to fit the values of β and R_s ; from an observational viewpoint, it is easy to measure $V_c(r)$, which could again be used to fit β and R_s .

The potential inside a spherical halo is then given as

$$\Phi(r) = \int_0^r \frac{GM(r')}{r'^2} dr' + C \quad (39)$$

in which $GM(r)/r^2$ is the gravitational force and C is a constant to be fixed using the fact that $\Phi(r = \infty) = \Phi_\infty$ where Φ_∞ is the value of the potential far from the halo.

Using the formula for $GM(r)/r^2$ given in Eq. (38) it is

not difficult to find that

$$\int_0^r \frac{GM(r')}{r'^2} dr' = 4\pi G\beta\rho_c R_s^3 \left[\frac{1}{R_s} - \frac{\ln\left(1 + \frac{r}{R_s}\right)}{r} \right]$$

and so

$$C = \Phi_\infty - 4\pi G\beta\rho_c R_s^2. \quad (40)$$

Then it follows that

$$\Phi(r) = \Phi_\infty - 4\pi G\beta\rho_c \frac{R_s^3}{r} \ln\left(1 + \frac{r}{R_s}\right). \quad (41)$$

If the halo is *isolated*, then $\Phi_\infty = 0$ and we get

$$\Phi(r) = -4\pi G\beta\rho_c \frac{R_s^3}{r} \ln\left(1 + \frac{r}{R_s}\right). \quad (42)$$

However, in N -body simulations, we have a large number of dark matter halos and no halo is totally isolated from the others. In such situations, Φ_∞ in Eq. (41) should be replaced by Φ_* , which is the potential produced by other halos inside the considered halo (note that in practice Φ_* could be position dependent as well, but for simplicity we assume that it is a constant, which is a good assumption

for many halos). Then we get

$$a\sqrt{\kappa}\delta\varphi(r) = -\frac{2\gamma\sqrt{\kappa_*\bar{\varphi}}}{1 + \frac{8\gamma^2\kappa_*\bar{\varphi}}{1+\gamma\kappa_*\bar{\varphi}}} \times \left[\Phi_* - 4\pi G\beta\rho_c \frac{R_s^3}{r} \ln\left(1 + \frac{r}{R_s}\right) \right]. \quad (43)$$

Eq. (43) provides a neat analytical formula for $a\sqrt{\kappa}\delta\varphi$ in halos, but unfortunately in most cases it cannot be used directly because we lack information about Φ_* . We will then be forced either to fit Φ_* as a free parameter, or tune its value to match simulations or observations. In this work we shall take the second approach, and we find that with an appropriate value of Φ_* and with values of β and R_s fitted using Eq. (38), Eq. (43) agrees with numerical results for most halos.

Some examples are shown in Fig. 9, in which we have computed $a\sqrt{\kappa}\delta\varphi(r)$ using four different methods: direct N -body simulation results (big green crosses), Eq. (43) with $\Phi_* = 0$ (solid curves), Eq. (43) with Φ_* properly tuned (dashed curves) and Eq. (35) with Φ directly from N -body simulations (small red asterisks). Clearly the crosses and asterisks agree with each other very well, which is another demonstration that Eq. (35) is a very good approximation (cf. Fig. 3). The solid curves differ significantly from the numerical results, showing that Φ_* is actually nonzero; once it is appropriately tuned, then Eq. (43) (dashed curves) agree with the numerical results very well for all the chosen halos. Eq. (43) therefore provides a useful analytical formula which might aid in general analysis.

We also notice that across the halos, the variation of $a\sqrt{\kappa}\delta\varphi$ is typically $\lesssim \mathcal{O}(10^{-6} \sim 10^{-5})$. Such a small variation is unlikely to be detectable using current observational instruments, and thus we do not expect special constraints based on the spatial variation of G . However, we stress that the above result is only for a class of extended quintessence models, and although we expect it to be valid for other potentials which are not particularly nonlinear, the situation could be dramatically changed in cases where the potential or coupling function becomes highly nonlinear. Such models require a more careful treatment, including some of the approximations adopted above becoming invalid, and are thus beyond the scope of the current work.

5. SUMMARY AND CONCLUSION

In summary, in this paper we have described a numerical method to study extended quintessence models, where the quintessence field has a scalar-tensor type of coupling to the curvature, from background cosmology to nonlinear structure formation, and discussed the regime of validity of the method. Instead of assuming a Yukawa force due to scalar coupling or simply a rescaling of gravitational constant, we have solved the scalar field and its spatial variation explicitly from their equation of motion. This is a necessary step in general to obtain trustworthy results and check various approximations which are made to simplify the computation.

As specific examples, we apply the above method to a specific class of models with inverse power-law potential Eq. (10) and non-minimal coupling Eq. (11). The analysis of the background cosmology and its linear per-

turbation shows that for these models the effective gravitational 'constants' relevant for the cosmic expansion rate and structure formation are either both increased or both decreased (albeit by slightly different amounts). The two effects compete and cancel each other, and as a result the net effect on large scale structure in the linear regime is weak (cf. Fig. 2). We then investigated whether a more significant signature of the scalar field could be imprinted in the nonlinear regime of structure formation.

The nonlinear matter power spectra plotted in Fig. 5 suggests that the effect of the scalar field is more significant in the nonlinear regime. For the models with $\alpha = 0.5$ (*i.e.*, steeper potential), the scalar field changes (either increases or decreases) the matter power spectrum by $30 \sim 50\%$ on small scales with respect to the Λ CDM prediction. Going to nonlinear scales thus greatly enhances the power of constraining such models using cosmological data. However, the power is more limited for models with $\alpha = 0.1$ (*i.e.*, shallower potential); their matter power spectra are very similar to the Λ CDM results. Of the two competing effects mentioned above, we find that the modified background expansion rate is more influential on nonlinear scales.

Properties of mass functions (cf. Fig. 6) are in qualitative agreement with what we have seen in the matter power spectrum, with the extended quintessence models producing less massive halos than Λ CDM. Therefore galaxy cluster counts could place meaningful constraints on such models as well. But as the matter power spectrum, the mass function for the models with $\alpha = 0.1$ (*i.e.*, shallower potential) is very similar to the Λ CDM result.

The halo density profiles for the extended quintessence models are shown to be well described by the well-known NFW formula (cf. Fig. 7, 8). In Fig. 8 we have shown the results of the fitting for the 80 most massive halos from each simulation. Consistent with the findings in Figs. 5 and 6, we see that the concentration parameter c_{NFW} for the halos in the $\alpha = 0.1$ models is almost the same as for the Λ CDM halos. But for $\alpha = 0.5$, the $\gamma = -0.2$ and $\gamma = 0.2$ cases predict overall bigger and smaller c_{NFW} than Λ CDM, respectively. Furthermore, Fig. 8 shows clearly that the halos in the $(\alpha, \gamma) = (0.5, 0.2)$ model are consistently less massive than those in Λ CDM, as suggested by the mass function plots.

Scalar-tensor theories (which the extended quintessence models belong to) are often studied in the context of varying gravitational constant, and so we have also considered the spatial variations (time variation has been investigated in detail elsewhere and will not be repeated here) in the scalar field (or equivalently the locally measured gravitational constant κ_{\oplus}). We first showed in Fig. 3 that the approximation that the scalar field perturbation $a\sqrt{\kappa_*}\delta\varphi$ is proportional to the gravitational potential Φ [cf. Eq. (35)] is fairly accurate. Then, based on this fact and using the NFW density profile, we derive an analytical formula for $a\sqrt{\kappa_*}\delta\varphi(r)$ in spherical halos, in which the parameters are obtained by fitting the NFW circular velocity profile. We have shown that this formula could be tuned to fit the numerical results pretty well for most halos (cf. Fig. 9).

Fig. 9 indicates that the spatial variation of $a\sqrt{\kappa_*}\delta\varphi$ across halos is at most of order 10^{-5} , which is far smaller

than the background value $\sqrt{\kappa_*}\bar{\varphi} \sim \mathcal{O}(0.1-1)$. Therefore the spatial variation of κ_\oplus is expected to be of order 10^{-5} or less in the halos, which is difficult to detect.

The smallness of $a\sqrt{\kappa_*}\delta\varphi$ also implies that the approximations we have made to simplify the simulations are valid. For example, because $|a\sqrt{\kappa_*}\delta\varphi| \ll 1$, which means it is reasonable to ignore the contribution from $\delta\dot{\varphi}, \delta\ddot{\varphi}$ to the total density/pressure perturbation, we can also replace φ by $\bar{\varphi}$ in the coefficients of perturbation quantities such as $\bar{\partial}_x^2\Phi$ and $\bar{\partial}_x^2(a\sqrt{\kappa_*}\delta\varphi)$. Moreover, the quasi static limit, *i.e.*, neglecting $\delta\dot{\varphi}, \delta\ddot{\varphi}$ compared to $\bar{\partial}_x^2(a\sqrt{\kappa_*}\delta\varphi)$, is guaranteed to work well.

One of the most important results of this work is that it confirms explicitly that, for a broad range of extended quintessence models, the N -body simulation reduces to modifying the background expansion rate and rescaling the effective gravitational constant based on the the background value of φ . This works to quite high accuracy and thus there is no need to solve the scalar field equation of motion explicitly, which is particularly time-consuming for large simulations. However, we expect this approximation to break down in extreme situa-

tions where the potential (or perhaps the coupling function) becomes highly nonlinear, and then both our results and method might have to be revised.

The work described in this paper has been performed on TITAN, the computing facilities at the University of Oslo in Norway; coding and testing are done on the SARA supercomputer in the Netherlands, supported by the European Community Research Infrastructure Action under the FP8 "Structuring the European Research Area" Programme. Postprocessing is done on COSMOS, the UK's National Cosmology Supercomputer. We have used POWMES (Colombi *et al.* 2008) to measure the matter power spectrum from output particle distribution, and a modified version of CAMB (Lewis, Challinor & Lasenby 2000) for our linear perturbation computation. We thank David Wands for discussions. B. Li is supported by the Research Fellowship at Queens' College, Cambridge, and the Science and Technology Facility Council of the United Kingdom. DFM thanks the Research Council of Norway FRINAT grant 197251/V30.

APPENDIX

USEFUL EXPRESSIONS

In this appendix we list some useful expressions in the derivation of our equations, because different researchers use different conventions.

Our line element is

$$ds^2 = a^2(1 + 2\phi)d\tau^2 - a^2(1 - 2\psi)\gamma_{ij}dx^i dx^j \quad (\text{A1})$$

where τ is the conformal time, x^i is the comoving coordinate and γ_{ij} the metric in the 3-space (with i, j running over 1, 2, 3). The nonzero Christoffel symbols, up to first order in perturbation, are

$$\begin{aligned} \Gamma_{00}^0 &= \frac{a'}{a} + \phi', & \Gamma_{0i}^0 &= \phi_{,i} \\ \Gamma_{0j}^i &= \left(\frac{a'}{a} - \psi'\right)\delta^i_j, & \Gamma_{00}^i &= \phi^{,i} \\ \Gamma_{ij}^0 &= \frac{a'}{a}(1 - 2\phi - 2\psi)\gamma_{ij} - \psi'\gamma_{ij} \\ \Gamma_{jk}^i &= -\psi_{,k}\delta^i_j - \psi_{,j}\delta^i_k + \psi^{,i}\gamma_{jk} \end{aligned} \quad (\text{A2})$$

where a comma denotes a partial derivative with respect to the comoving coordinate, and indices are raised and lowered by γ^{ij} and γ_{ij} respectively. $' \equiv d/d\tau$.

The Ricci tensor is

$$R_{ab} = \Gamma_{ab,c}^c - \Gamma_{ac,b}^c + \Gamma_{cd}^c \Gamma_{ab}^d - \Gamma_{cb}^d \Gamma_{ad}^c \quad (\text{A3})$$

and its components up to first order in perturbation are

$$\begin{aligned} R_{00} &= \phi^{,i}_{,i} - 3 \left[\frac{a''}{a} - \left(\frac{a'}{a}\right)^2 \right] + 3\psi'' + 3\frac{a'}{a}(\phi' + \psi'), \\ R_{0i} &= 2\psi'_{,i} + 2\frac{a'}{a}\phi_{,i}, \\ R_{ij} &= -\psi''\gamma_{ij} - \frac{a'}{a}(\phi' + 5\psi')\gamma_{ij} - (\phi - \psi)_{,ij} \\ &\quad + \left[\frac{a''}{a} + \left(\frac{a'}{a}\right)^2 \right] (1 - 2\phi - 2\psi)\gamma_{ij} + \psi^{,k}_{,k}\gamma_{ij}. \end{aligned}$$

The Ricci scalar R and relevant components of Einstein tensor $G_{ab} = R_{ab} - \frac{1}{2}g_{ab}R$ are

$$R = \frac{6}{a^2} \left[\psi'' - \frac{a''}{a}(1-2\phi) + \frac{a'}{a}(\phi' + 3\psi') \right] - \frac{1}{a^2} \left[4\psi_{,i}^{\prime i} - 2\phi_{,i}^{\prime i} \right], \quad (\text{A4})$$

$$G^0_0 = \frac{3}{a^2} \left(\frac{a'}{a} \right)^2 (1-2\phi) - \frac{6}{a^2} \frac{a'}{a} \psi' + \frac{2}{a^2} \psi_{,i}^{\prime i}, \quad (\text{A5})$$

$$G^i_j = \frac{1}{a^2} \left[-2\psi'' - 2\frac{a'}{a}(\phi' + 2\psi') - (\phi - \psi)_{,k}^{\prime k} \right] \delta^i_j + \frac{1}{a^2} \left[2\frac{a''}{a} - \left(\frac{a'}{a} \right)^2 \right] (1-2\phi)\delta^i_j + \frac{1}{a^2} (\phi - \psi)_{,j}^{\prime i}. \quad (\text{A6})$$

DISCRETE EQUATIONS FOR THE N -BODY SIMULATIONS

In the MLAPM code the Poisson equation Eq. (25) is (and in our modified code the scalar field equation of motion Eq. (20) will also be) solved on discretised grid points, so we must develop the discrete versions of Eqs. (20, 25) to be implemented in the code. Before doing that, we note that Eqs. (20, 25) are not independent but are coupled together, which could further complicate the solver. As a result, we should first decouple them by eliminating $\vec{\partial}_x^2 (a\sqrt{\kappa_*}\delta\varphi)$ ($\vec{\partial}_x^2\Phi$) from the equation for Φ ($\delta\varphi$). This is easy to do and the resulted equations are respectively

$$\begin{aligned} \left[1 + \frac{6\gamma^2\kappa_*\bar{\varphi}^2}{1 + \gamma\kappa_*\bar{\varphi}^2} \right] c^2 \vec{\partial}_x^2 (a\sqrt{\kappa_*}\delta\varphi) = & -6\gamma(\mathcal{H}' + \mathcal{H}^2) a\sqrt{\kappa_*}\delta\varphi - 3\alpha\lambda H_0^2 a^3 \left[\frac{1}{(\sqrt{\kappa_*}\varphi)^\alpha} - \frac{1}{(\sqrt{\kappa_*}\bar{\varphi})^\alpha} \right] \\ & - 3\gamma\sqrt{\kappa_*}\bar{\varphi} (1 + \gamma\kappa_*\bar{\varphi}_0^2) \Omega_m H_0^2 \left[\frac{\rho_c}{1 + \gamma\kappa_*\varphi^2} - \frac{1}{1 + \gamma\kappa_*\bar{\varphi}^2} \right] \\ & + 6\gamma\sqrt{\kappa_*}\bar{\varphi}\lambda H_0^2 a^3 \left[\frac{1}{(1 + \gamma\kappa_*\varphi^2)(\sqrt{\kappa_*}\varphi)^\alpha} - \frac{1}{(1 + \gamma\kappa_*\bar{\varphi}^2)(\sqrt{\kappa_*}\bar{\varphi})^\alpha} \right] \\ & - 2\gamma\sqrt{\kappa_*}\bar{\varphi}a \left[(1 + 3\gamma)\kappa_*\bar{\varphi}'^2 + 3\gamma\kappa_*\bar{\varphi}\bar{\varphi}'' \right] \left[\frac{1}{1 + \gamma\kappa_*\varphi^2} - \frac{1}{1 + \gamma\kappa_*\bar{\varphi}^2} \right] \end{aligned} \quad (\text{B1})$$

for the scalar field, and

$$\begin{aligned} & \frac{1 + \gamma\kappa_*\bar{\varphi}^2 + 6\gamma^2\kappa_*\bar{\varphi}^2}{1 + \gamma\kappa_*\bar{\varphi}^2 + 8\gamma^2\kappa_*\bar{\varphi}^2} \vec{\partial}_x^2 \Phi \\ = & \frac{3}{2} (1 + \gamma\kappa_*\bar{\varphi}_0^2) \Omega_m H_0^2 \left[\frac{\rho_c}{1 + \gamma\kappa_*\varphi^2} - \frac{1}{1 + \gamma\kappa_*\bar{\varphi}^2} \right] - 3\lambda H_0^2 a^3 \left[\frac{1}{(1 + \gamma\kappa_*\varphi^2)(\sqrt{\kappa_*}\varphi)^\alpha} - \frac{1}{(1 + \gamma\kappa_*\bar{\varphi}^2)(\sqrt{\kappa_*}\bar{\varphi})^\alpha} \right] \\ & + a \left[(1 + 3\gamma)\kappa_*\bar{\varphi}'^2 + 3\gamma\kappa_*\bar{\varphi}\bar{\varphi}'' \right] \left[\frac{1}{1 + \gamma\kappa_*\varphi^2} - \frac{1}{1 + \gamma\kappa_*\bar{\varphi}^2} \right] + \frac{6\gamma^2\sqrt{\kappa_*}\bar{\varphi}}{1 + \gamma\kappa_*\bar{\varphi}^2 + 8\gamma^2\kappa_*\bar{\varphi}^2} (\mathcal{H}' + \mathcal{H}^2) a\sqrt{\kappa_*}\delta\varphi \\ & + \frac{3\gamma\alpha\lambda\sqrt{\kappa_*}\bar{\varphi}}{1 + \gamma\kappa_*\bar{\varphi}^2 + 8\gamma^2\kappa_*\bar{\varphi}^2} H_0^2 a^3 \left[\frac{1}{(\sqrt{\kappa_*}\varphi)^{1+\alpha}} - \frac{1}{(\sqrt{\kappa_*}\bar{\varphi})^{1+\alpha}} \right] \end{aligned} \quad (\text{B2})$$

for the gravitational potential.

Introducing the variable u (cf. Sect. 2.3), the Poisson equation becomes

$$\begin{aligned}
& \frac{1 + \gamma\kappa_*\bar{\varphi}^2 + 6\gamma^2\kappa_*\bar{\varphi}^2}{1 + \gamma\kappa_*\bar{\varphi}^2 + 8\gamma^2\kappa_*\bar{\varphi}^2} \nabla^2 \Phi_c \tag{B3} \\
&= \frac{3}{2} (1 + \gamma\kappa_*\bar{\varphi}_0^2) \Omega_m \left[\frac{\rho_c}{1 + \gamma \left(\sqrt{\kappa_*}\bar{\varphi} + \frac{B^2 H_0^2}{ac^2} u \right)^2} - \frac{1}{1 + \gamma\kappa_*\bar{\varphi}^2} \right] \\
&\quad - 3\lambda a^3 \left[\frac{1}{1 + \gamma \left(\sqrt{\kappa_*}\bar{\varphi} + \frac{B^2 H_0^2}{ac^2} u \right)^2} \frac{1}{\left(\sqrt{\kappa_*}\bar{\varphi} + \frac{B^2 H_0^2}{ac^2} u \right)^\alpha} - \frac{1}{1 + \gamma\kappa_*\bar{\varphi}^2} \frac{1}{\left(\sqrt{\kappa_*}\bar{\varphi} \right)^\alpha} \right] \\
&\quad + a \left[(1 + 3\gamma) \frac{\kappa_*\bar{\varphi}^2}{H_0^2} + 3\gamma\sqrt{\kappa_*}\bar{\varphi} \frac{\sqrt{\kappa_*}\bar{\varphi}''}{H_0^2} \right] \left[\frac{1}{1 + \gamma \left(\sqrt{\kappa_*}\bar{\varphi} + \frac{B^2 H_0^2}{ac^2} u \right)^2} - \frac{1}{1 + \gamma\kappa_*\bar{\varphi}^2} \right] \\
&\quad + \frac{\gamma\sqrt{\kappa_*}\bar{\varphi}}{1 + \gamma\kappa_*\bar{\varphi}^2 + 8\gamma^2\kappa_*\bar{\varphi}^2} \left\{ 6\gamma \left[\frac{\mathcal{H}'}{H_0^2} + \frac{\mathcal{H}^2}{H_0^2} \right] \frac{(BH_0)^2}{c^2} u + 3\alpha\lambda a^3 \left[\frac{1}{\left(\sqrt{\kappa_*}\bar{\varphi} + \frac{B^2 H_0^2}{ac^2} u \right)^{1+\alpha}} - \frac{1}{\left(\sqrt{\kappa_*}\bar{\varphi} \right)^{1+\alpha}} \right] \right\} \tag{B4}
\end{aligned}$$

where λ is defined in Sect. 2.3 and is a constant of $\mathcal{O}(1)$. We have also used the code unit for other quantities. This equation contains u , which must be solved from the scalar field equation of motion.

The scalar field equation of motion can be similarly written. In order that the equation can be integrated into MLAPM, we need to discretise it for the application of Newton-Gauss-Seidel relaxation method. This means writing down a discrete version of this equation on a uniform grid with grid spacing h . Suppose we want to achieve second-order precision, as is in the default Poisson solver of MLAPM, then $\nabla^2 u$ in one dimension can be

written as

$$\nabla^2 u \rightarrow \nabla^2 u_j = \frac{u_{j+1} + u_{j-1} - 2u_j}{h^2} \tag{B5}$$

where a subscript j means that the quantity is evaluated on the j -th point. The generalisation to three dimensions is straightforward.

The discrete version of the equation of motion for u is then

$$L^h(u_{i,j,k}) = 0, \tag{B6}$$

in which

$$\begin{aligned}
L^h(u_{i,j,k}) &= \frac{1 + \gamma\kappa_*\bar{\varphi}^2 + 6\gamma^2\kappa_*\bar{\varphi}^2}{1 + \gamma\kappa_*\bar{\varphi}^2} \frac{1}{h^2} [u_{i+1,j,k} + u_{i-1,j,k} + u_{i,j+1,k} + u_{i,j-1,k} + u_{i,j,k+1} + u_{i,j,k-1} - 6u_{i,j,k}] \\
&\quad + 3\gamma\sqrt{\kappa_*}\bar{\varphi} (1 + \gamma\kappa_*\bar{\varphi}_0^2) \Omega_m \left[\frac{\rho_c}{1 + \gamma \left(\sqrt{\kappa_*}\bar{\varphi} + \frac{B^2 H_0^2}{ac^2} u_{i,j,k} \right)^2} - \frac{1}{1 + \gamma\kappa_*\bar{\varphi}^2} \right] \\
&\quad + 3\alpha\lambda a^3 \left[\frac{1}{\left(\sqrt{\kappa_*}\bar{\varphi} + \frac{B^2 H_0^2}{ac^2} u_{i,j,k} \right)^{1+\alpha}} - \frac{1}{\left(\sqrt{\kappa_*}\bar{\varphi} \right)^{1+\alpha}} \right] + 6\gamma \frac{\mathcal{H}' + \mathcal{H}^2}{H_0^2} \frac{B^2 H_0^2}{c^2} u_{i,j,k} \\
&\quad - 6\gamma\sqrt{\kappa_*}\bar{\varphi} \lambda a^3 \left[\frac{1}{1 + \gamma \left(\sqrt{\kappa_*}\bar{\varphi} + \frac{B^2 H_0^2}{ac^2} u_{i,j,k} \right)^2} \frac{1}{\left(\sqrt{\kappa_*}\bar{\varphi} + \frac{B^2 H_0^2}{ac^2} u_{i,j,k} \right)^\alpha} - \frac{1}{1 + \gamma\kappa_*\bar{\varphi}^2} \frac{1}{\left(\sqrt{\kappa_*}\bar{\varphi} \right)^\alpha} \right] \\
&\quad + 2\gamma\sqrt{\kappa_*}\bar{\varphi} a \left[(1 + 3\gamma) \frac{\kappa_*\bar{\varphi}^2}{H_0^2} + 3\gamma\sqrt{\kappa_*}\bar{\varphi} \frac{\sqrt{\kappa_*}\bar{\varphi}''}{H_0^2} \right] \left[\frac{1}{1 + \gamma \left(\sqrt{\kappa_*}\bar{\varphi} + \frac{B^2 H_0^2}{ac^2} u_{i,j,k} \right)^2} - \frac{1}{1 + \gamma\kappa_*\bar{\varphi}^2} \right] \tag{B7}
\end{aligned}$$

Then, the Newton-Gauss-Seidel iteration says that we can obtain a new (and often more accurate) solution of u , $u_{i,j,k}^{\text{new}}$, using our knowledge about the old (and less

accurate) solution $u_{i,j,k}^{\text{old}}$ via

$$u_{i,j,k}^{\text{new}} = u_{i,j,k}^{\text{old}} - \frac{L^h(u_{i,j,k}^{\text{old}})}{\partial L^h(u_{i,j,k}^{\text{old}}) / \partial u_{i,j,k}}. \tag{B8}$$

The old solution will be replaced by the new solution to $u_{i,j,k}$ once the new solution is ready, using the red-black Gauss-Seidel sweeping scheme. Note that

$$\begin{aligned}
\frac{\partial L^h(u_{i,j,k})}{\partial u_{i,j,k}} = & -\frac{1 + \gamma\kappa_*\bar{\varphi}^2 + 6\gamma^2\kappa_*\bar{\varphi}^2}{1 + \gamma\kappa_*\bar{\varphi}^2} \frac{6}{h^2} + 6\gamma \frac{\mathcal{H}'}{H_0^2} \frac{B^2 H_0^2}{c^2} - \frac{3\alpha(1 + \alpha)\lambda a^2 (BH_0/c)^2}{\left(\sqrt{\kappa_*}\bar{\varphi} + \frac{B^2 H_0^2}{ac^2} u_{i,j,k}\right)^{2+\alpha}} \\
& - 6\gamma^2 \frac{B^2 H_0^2}{ac^2} \sqrt{\kappa_*}\bar{\varphi} (1 + \gamma\kappa_*\bar{\varphi}_0^2) \Omega_m \rho_c \frac{\sqrt{\kappa_*}\bar{\varphi} + \frac{B^2 H_0^2}{ac^2} u_{i,j,k}}{\left[1 + \gamma \left(\sqrt{\kappa_*}\bar{\varphi} + \frac{B^2 H_0^2}{ac^2} u_{i,j,k}\right)^2\right]^2} \\
& + 12\gamma^2 \frac{B^2 H_0^2}{ac^2} \lambda \sqrt{\kappa_*}\bar{\varphi} a^3 \frac{\sqrt{\kappa_*}\bar{\varphi} + \frac{B^2 H_0^2}{ac^2} u_{i,j,k}}{\left[1 + \gamma \left(\sqrt{\kappa_*}\bar{\varphi} + \frac{B^2 H_0^2}{ac^2} u_{i,j,k}\right)^2\right]^2} \frac{1}{\left(\sqrt{\kappa_*}\bar{\varphi} + \frac{B^2 H_0^2}{ac^2} u_{i,j,k}\right)^\alpha} \\
& + 6\alpha\gamma \frac{B^2 H_0^2}{ac^2} \lambda \sqrt{\kappa_*}\bar{\varphi} a^3 \frac{1}{1 + \gamma \left(\sqrt{\kappa_*}\bar{\varphi} + \frac{B^2 H_0^2}{ac^2} u_{i,j,k}\right)^2} \frac{1}{\left(\sqrt{\kappa_*}\bar{\varphi} + \frac{B^2 H_0^2}{ac^2} u_{i,j,k}\right)^{1+\alpha}} \\
& - 4\gamma^2 \frac{B^2 H_0^2}{c^2} \sqrt{\kappa_*}\bar{\varphi} \left[(1 + 3\gamma) \frac{\kappa_*\bar{\varphi}'^2}{H_0^2} + 3\gamma\sqrt{\kappa_*}\bar{\varphi} \frac{\sqrt{\kappa_*}\bar{\varphi}''}{H_0^2} \right] \frac{\sqrt{\kappa_*}\bar{\varphi} + \frac{B^2 H_0^2}{ac^2} u_{i,j,k}}{\left[1 + \gamma \left(\sqrt{\kappa_*}\bar{\varphi} + \frac{B^2 H_0^2}{ac^2} u_{i,j,k}\right)^2\right]^2}. \quad (\text{B9})
\end{aligned}$$

In principle, if we start from a high redshift, then the initial guess of $u_{i,j,k}$ for the relaxation can be so chosen that the initial value of φ in all space is equal to the background value $\bar{\varphi}$, because at this time we expect this to be approximately true any way. At subsequent time-steps we could use the solution for $u_{i,j,k}$ from the previous time-step as our initial guess. If the timestep is small enough then we would expect u to change only slightly between consecutive timesteps so that such a guess will be good enough for the iterations to converge quickly.

ALGORITHM TO SOLVE THE BACKGROUND EVOLUTION

Here we give our formulae and algorithm for the background field equations which can also be applied to linear Boltzmann codes such as **CAMB**. Throughout this Appendix we use the conformal time τ instead of the physical time t , and $' \equiv d/d\tau$, $\mathcal{H} \equiv a'/a$. All quantities appearing here are background ones unless stated otherwise.

For convenience, we will work with dimensionless quantities and define $\psi \equiv \sqrt{\kappa_*}\varphi$ and $N \equiv \ln a$ so that

$$\psi' = \mathcal{H} \frac{d\psi}{dN}, \quad (\text{C1})$$

$$\psi'' = \mathcal{H}^2 \frac{d^2\psi}{dN^2} + \mathcal{H}' \frac{d\psi}{dN}. \quad (\text{C2})$$

With these definitions it is straightforward to show that the scalar field equation of motion can be expressed as

$$\begin{aligned}
& \left(\frac{\mathcal{H}}{\mathcal{H}_0}\right)^2 \frac{d^2\psi}{dN^2} + \left(2\frac{\mathcal{H}^2}{\mathcal{H}_0^2} + \frac{\mathcal{H}'}{\mathcal{H}_0^2}\right) \frac{d\psi}{dN} \\
& + \frac{\kappa_*}{\mathcal{H}_0^2} a^2 \frac{\partial V(\psi)}{\partial \psi} - 3 \left(\frac{\mathcal{H}'}{\mathcal{H}_0^2} + \frac{\mathcal{H}^2}{\mathcal{H}_0^2}\right) \frac{\partial f(\psi)}{\partial \psi} = 0, \quad (\text{C3})
\end{aligned}$$

where \mathcal{H}_0 is the current value of \mathcal{H} .

Obviously we need to know how to compute the quantities $\mathcal{H}/\mathcal{H}_0$ and $\mathcal{H}'/\mathcal{H}_0$ as well. For $\mathcal{H}/\mathcal{H}_0$, we start with the Friedmann equation

$$\begin{aligned}
3\mathcal{H}^2 = & \frac{1}{1+f} \kappa_* [\rho_m + \rho_r + V(\psi)] a^2 \\
& + \frac{1}{1+f} \left[\frac{1}{2} \left(\frac{d\psi}{dN}\right)^2 - 3 \frac{df}{d\psi} \frac{d\psi}{dN} \right] \mathcal{H}^2, \quad (\text{C4})
\end{aligned}$$

where ρ_m and ρ_r are the energy densities for matter and radiation respectively. We define the fractional energy densities for matter and radiation respectively as

$$\Omega_m \equiv \frac{\kappa_{eff} \rho_{m0}}{3\mathcal{H}_0^2} = \frac{1}{1+f_0} \frac{\kappa_* \rho_{m0}}{3\mathcal{H}_0^2}, \quad (\text{C5})$$

$$\begin{aligned}
\Omega_r & \equiv \frac{\kappa_{\oplus 0} \rho_{r0}}{3\mathcal{H}_0^2} \\
& = \frac{1}{1+f_0} \frac{2(1+f_0) + 4 \left(\frac{df}{d\psi}\right)_0^2}{2(1+f_0) + 3 \left(\frac{df}{d\psi}\right)_0^2} \frac{\kappa_* \rho_{r0}}{3\mathcal{H}_0^2}, \quad (\text{C6})
\end{aligned}$$

where a subscript $_0$ means the present-day value. Notice the difference between these definitions, which comes from the different treatments for radiation and matter in numerical codes such as **CAMB**. For radiation, *e.g.*, photon, we know the present temperature of the CMB and thus its exact energy density ρ_{r0} , as well as the locally measured value of gravitational constant $\kappa_{\oplus 0}$ (which in scalar-tensor theories is in general different from κ_*) and current Hubble expansion rate \mathcal{H}_0 , and so the definition Eq. (C6) comes out naturally, where we have used the relation between κ_* and κ_{\oplus} ¹. For matter, the fractional

energy density is to be interpreted from the cosmological observables such as CMB and large scale structure, which are obviously different in Λ CDM and scalar-tensor theories; consequently there is some freedom in defining it and we make it as in Eq. (C5).

Then, remembering that

$$\rho_m \propto a^{-3}, \quad (\text{C7})$$

$$\rho_r \propto a^{-4}, \quad (\text{C8})$$

we have

$$\left(\frac{\mathcal{H}}{\mathcal{H}_0}\right)^2 = \frac{\frac{\kappa_*}{\kappa_{\oplus 0}} \Omega_r a^{-2} + (1+f_0) \Omega_m a^{-1} + \frac{\kappa_* V a^2}{3\mathcal{H}_0^2}}{1+f + \frac{df}{d\psi} \frac{d\psi}{dN} - \frac{1}{6} \left(\frac{d\psi}{dN}\right)^2}, \quad (\text{C9})$$

in which (where both κ_* and $\kappa_{\oplus 0}$ are constants, and $\kappa_{\oplus 0}$ is the present value of κ_{\oplus})

$$\frac{\kappa_*}{\kappa_{\oplus 0}} = (1+f_0) \frac{2(1+f_0) + 3\left(\frac{df}{d\psi}\right)_0^2}{2(1+f_0) + 4\left(\frac{df}{d\psi}\right)_0^2}. \quad (\text{C10})$$

For $\mathcal{H}'/\mathcal{H}_0$, we use the Raychaudhuri equation

$$\begin{aligned} \mathcal{H}' &= -\frac{1}{6} \kappa_* (\rho + 3p) a^2 \\ &= -\frac{1}{6} \frac{1}{1+f} \kappa_* [\rho_m + 2\rho_r - 2V(\psi)] a^2 \\ &\quad - \frac{1}{6} \frac{1}{1+f} \left(2 + 3 \frac{d^2 f}{d\psi^2}\right) \left(\frac{d\psi}{dN}\right)^2 \mathcal{H}^2 \\ &\quad - \frac{1}{2} \frac{1}{1+f} \frac{df}{d\psi} \left(\frac{d\psi}{dN} \mathcal{H}' + \frac{d^2 \psi}{dN^2} \mathcal{H}^2\right). \end{aligned} \quad (\text{C11})$$

As in the above, dividing this by \mathcal{H}_0^2 and rearranging, we obtain

$$\begin{aligned} \frac{\mathcal{H}'}{\mathcal{H}_0^2} &= -\frac{\frac{1}{2} \left[(1+f_0) \Omega_m a^{-1} + 2 \frac{\kappa_*}{\kappa_{\oplus 0}} \Omega_r a^{-2}\right] - \frac{\kappa_* V a^2}{3\mathcal{H}_0^2}}{1+f + \frac{1}{2} \frac{df}{d\psi} \frac{d\psi}{dN}} \\ &\quad - \frac{\frac{1}{2} \frac{df}{d\psi} \frac{d^2 \psi}{dN^2} + \left(\frac{1}{3} + \frac{1}{2} \frac{d^2 f}{d\psi^2}\right) \left(\frac{d\psi}{dN}\right)^2}{1+f + \frac{1}{2} \frac{df}{d\psi} \frac{d\psi}{dN}} \frac{\mathcal{H}^2}{\mathcal{H}_0^2}. \end{aligned} \quad (\text{C12})$$

Substituting Eqs. (C9, C12) into Eq. (C3), we finally arrive at

$$\begin{aligned} \frac{1+f + \frac{3}{2} \left(\frac{df}{d\psi}\right)^2}{1+f + \frac{1}{2} \frac{df}{d\psi} \frac{d\psi}{dN}} A \frac{d^2 \psi}{dN^2} + (2A+B) \frac{d\psi}{dN} \\ + \frac{\kappa_*}{\mathcal{H}_0^2} \frac{dV}{d\psi} a^2 - 3(A+B) \frac{df}{d\psi} = 0, \end{aligned} \quad (\text{C13})$$

in which we have defined

$$A \equiv \frac{\mathcal{H}^2}{\mathcal{H}_0^2}, \quad (\text{C14})$$

$$B \equiv \frac{\mathcal{H}'}{\mathcal{H}_0^2} + \frac{\frac{1}{2} \frac{df}{d\psi} \frac{\mathcal{H}^2}{\mathcal{H}_0^2}}{1+f + \frac{1}{2} \frac{df}{d\psi} \frac{d\psi}{dN}} \frac{d^2 \psi}{dN^2}, \quad (\text{C15})$$

where A and B do not contain $d^2\psi/dN^2$, to lighten the notation.

When solving for φ (or ψ), we just use Eq. (C3) aided by Eqs. (C9, C12). It may appear then that, given any initial values for ψ_{ini} and $(d\psi/dN)_{\text{ini}}$, the evolution of φ is obtainable. However, Eq. (C9) is not necessarily satisfied for ψ evolved in such way. Instead, it constrains the initial condition ψ must start with, and the way it must subsequently evolve. This in turn is determined by the parameters λ, α, γ , since α, γ specify a model and are fixed once the model is chosen; the only concern is λ .

As for the initial conditions ψ_{ini} and $(d\psi/dN)_{\text{ini}}$, we have found that the subsequent evolution of ψ is rather insensitive to them. Thus, we choose $\psi_{\text{ini}} = (d\psi/dN)_{\text{ini}} = 0$ at some very early time (say N_{ini} corresponds to $a_{\text{ini}} = e^{N_{\text{ini}}} = 10^{-8}$) in all the models. Such a choice is clearly not only practical but also reasonable, given the fact that we expect that the scalar field starts high up the potential and rolls down subsequently.

As for λ , we use a trial-and-error method to find its value which ensures that (again subscript 0 indicates the current time)

$$\frac{\frac{\kappa_*}{\kappa_{\oplus 0}} \Omega_r + (1+f_0) \Omega_m + \frac{\kappa_* V_0}{3\mathcal{H}_0^2}}{1+f_0 + \left(\frac{df}{d\psi}\right)_0 \left(\frac{d\psi}{dN}\right)_0 - \frac{1}{6} \left(\frac{d\psi}{dN}\right)_0^2} = 1 \quad (\text{C16})$$

which comes from setting $a = 1$ in Eq. (C9).

We determine the correct value of λ for any given α, γ in this way using a trial-and-error routine, and then compute the values of ψ and $d\psi/dN$ for predefined values of N stored in an array. Their values at any time are then obtained using interpolation, and with these it is straightforward to compute other relevant quantities, such as $\mathcal{H}, \mathcal{H}'$ and φ , which are used in the linear perturbation computations.

REFERENCES

- Amendola, L. 2000, Phys. Rev. D62, 043511
—, 2004, Phys. Rev. D69, 103524
Baccigalupi, C., & Perrotta, F. 2000, Mon. Not. Roy. Astron. Soc., 314, 1
¹ (Massless) neutrinos are treated similarly, but the neutrino background has a temperature lower than that of CMB, due to the energy transfer into photons during the electron-positron annihilation, but not into neutrinos which have decoupled by then.
Baccigalupi, C., Perrotta, F., & Matarrese, S. 2000, Phys. Rev. D61, 023507
Baldi, M. 2010, arXiv:1005.2188 [astro-ph.CO]
Baldi, M., & Pettorino, V. 2010, arXiv:1006.3761 [astro-ph.CO]
Baldi, M., Pettorino, V., Robbers, G., & Springel, V. 2010, Mon. Not. Roy. Astron. Soc., 403, 1684
Barrow, J. D., & Shaw, D. J. (2010), arXiv:1007.3086 [gr-qc]
Bean, R. 2001, Phys. Rev. D64, 123516
Bean, R., & Magueijo, J. 2001, Phys. Lett. B17, 177

- Bean, R., Flanagan, E. E., Laszlo, I., & Trodden, M. 2008, *Phys. Rev. D*78, 123514
- Bean, R., Flanagan, E. E., & Trodden, M. 2008, *Phys. Rev. D*78, 023009
- Brookfield, A. W., van de Bruck, C., Mota, D. F., & Tocchini-Valentini, D. 2006, *Phys. Rev. Lett.*, 96, 061301
- Boehmer, C. G., Caldera-Cabral, G., Lazkoz, R., & Maartens, R. 2008, *Phys. Rev. D*78, 023505
- Boehmer, C. G., Caldera-Cabral, G., Chan, N., Lazkoz, R., & Maartens, R. 2010, *Phys. Rev. D*81, 083003
- Clifton, T., Mota, D. F., & Barrow, J. D. 2005, *Mon. Not. Roy. Astron. Soc.*, 358, 601
- Colombi, S., Jaffe, A. H., Novikov, D., & Pichon, C. 2008, *Mon. Not. Roy. Astron. Soc.*, 393, 511
- Copeland, E. J., Sami, M., & Tsujikawa, S. 2006, *Int. J. Mod. Phys. D*15, 1753
- Farrar, G. R., & Rosen, R. A. 2007, *Phys. Rev. Lett.*, 98, 171302
- Fujii, Y., & Maeda, K. 2003, Cambridge University Press
- Hellwing, W. A., & Juszkiewicz, R. 2009, *Phys. Rev. D*80, 083522
- Hellwing, W. A., Knollmann, S. R., & Knebe, A. 2010, arXiv:1004.2929 [astro-ph.CO]
- Jesus, J. F., Santos, R. C., Alcaniz, J. S., & Lima, J. A. S. 2008, *Phys. Rev. D*78, 063514
- Kesden, M., & Kamionkowski, M. 2006a, *Phys. Rev. Lett.*, 97, 131303
- , 2006b, *Phys. Rev.*, D74, 083007
- Keselman, J. A., Nusser, A., & Peebles, P. J. E. 2009, *Phys. Rev. D*80, 063517
- , 2010, *Phys. Rev. D*81, 063521
- Knebe, A., & Gibson, B. K. 2004, *Mon. Not. Roy. Astron. Soc.*, 347, 1055
- Knebe, A., Green, A. & Binney, J. 2001, *Mon. Not. Roy. Astron. Soc.*, 325, 845
- Koivisto, T. 2005, *Phys. Rev. D*72, 043516
- Koivisto, T., & Mota, D. F. 2007, *Phys. Rev. D*75, 023518
- Lee, S., Liu, G. -C., & Ng, K. -W. 2006, *Phys. Rev. D*73, 083516
- Lewis, A., Challinor, A., & Lasenby, A. 2000, *Astrophys. J.*, 538, 473
- Li, B., & Barrow, J. D. 2010, arXiv:1005.4231 [astro-ph.CO]
- Li, B., & Zhao, H. 2009, *Phys. Rev. D*80, 044027
- , 2010, *Phys. Rev. D*81, 104047
- Li, B., Mota, D. F., & Barrow, J. D. (2010), in preparation.
- Maccio, A. V., Quercellini, C., Mainini, R., Amendola, L., & Bonometto, S. A. 2004, *Phys. Rev. D*69, 123516
- Manera, M., & Mota, D. F. 2006, *Mon. Not. Roy. Astron. Soc.*, 371, 1373
- Mangano, G., Miele, G., & Pettorino, V. 2003, *Mod. Phys. Lett. A*18, 831
- Mota, D. F. 2008, *JCAP*, 0809, 006
- Mota, D. F., Kristiansen, J. R., Koivisto, T., & Groeneboom, N. E. 2007, *Mon. Not. Roy. Astron. Soc.*, 382, 793
- Mota, D. F., Pettorino, V., Robbers, G., & Wetterich, C. 2008a, *Phys. Lett. B*663, 160
- Mota, D. F., & Shaw, D. J. 2006, *Phys. Rev. Lett.*, 97, 151102
- , 2007, *Phys. Rev. D*75, 063501
- Mota, D. F., Shaw, D. J., & Silk, J. 2008b, *Astrophys. J.*, 675, 29
- Mota, D. F., & van de Bruck, C. 2004, *Astron. Astrophys.*, 421, 71
- Navarro, J. F., Frenk, C. S., & White, S. D. M. 1996, *Astrophys. J.*, 462, 563
- Nunes, N. J., & Mota, D. F. 2006, *Mon. Not. Roy. Astron. Soc.*, 368, 751
- Nusser, A., Gubser, S. S., & Peebles, P. J. E. 2005, *Phys. Rev. D*71, 083505
- Perrotta, F., Baccigalupi, C. & Matarrese, S. 2000, *Phys. Rev. D*61, 023507
- Pettorino, V., & Baccigalupi, C. 2008, *Phys. Rev. D*77, 103003
- Pettorino, V., Baccigalupi, C., & Mangano, G. 2005, *J. Cosmo. Astropart. Phys.*, 0501, 014
- Riazuolo, A., & Uzan, J.-P. 2002, *Phys. Rev.*, D66, 023525
- Rodriguez-Meza, M. A. 2008a, *AIP Conf. Proc.*, 1083, 190
- , 2008b, *AIP Conf. Proc.*, 977, 302
- Rodriguez-Meza, M. A., Gonzalez-Morales, A. X., Gabbasov, R. F., & Cervantes-Cota, J. L. 2007, *J. Phys. Conf. Ser.*, 91, 012012
- Saracco, F., Pietroni, M., Tetradis, N., Pettorino, V., & Robbers, G. 2010, *Phys. Rev. D*82, 023528
- Shaw, D. J., & Mota, D. F. 2008, *Astrophys. J. Suppl.*, 174, 277
- Springel, V., & Farrar, G. 2007, *Mon. Not. Roy. Astron. Soc.*, 380, 911
- Wang, L.-M., Caldwell, R. R., Ostriker, J. P., & Steinhardt, P. J. 2000, *Astrophys. J.*, 530, 17
- Wintergerst, N., & Pettorino, V. (2010), arXiv: 1005.1278 [astro-ph.CO]
- Zhao, H., Maccio', A., Li, B., Hoekstra, H., & Feix, M. 2010, *Astrophys. J. Lett.*, 712, L179
- Zlatev, I., Wang, L.-M., & Steinhardt, P. J. 1999, *Phys. Rev. Lett.*, 82, 896